2019

Investigation of PS-PVD and EB-PVD Thermal Barrier Coatings Over Lifetime Using Synchrotron X-ray Diffraction

Matthew Northam
University of Central Florida

INVESTIGATION OF PS-PVD AND EB-PVD THERMAL BARRIER COATINGS OVER LIFETIME USING SYNCHROTRON X-RAY DIFFRACTION

by

MATTHEW NORTHAM
B.S. University of Central Florida, 2016

A thesis submitted in partial fulfilment of the requirements
for the degree of Master of Science
in the Department of Mechanical and Aerospace Engineering
in the College of Engineering and Computer Science
at the University of Central Florida
Orlando, Florida

Fall Term
2019

Major Professor: Seetha Raghavan

ABSTRACT

Extreme operating temperatures within the turbine section of jet engines require sophisticated methods of cooling and material protection. Thermal barrier coatings (TBCs) achieve this through a ceramic coating applied to a substrate material (nickel-based superalloy). Electron-beam physical vapor deposition (EB-PVD) is the industry standard coating used on jet engines. By tailoring the microstructure of an emerging deposition method, Plasma-spray physical vapor deposition (PS-PVD), similar microstructures to that of EB-PVD coatings can be fabricated, allowing the benefits of strain tolerance to be obtained while improving coating deposition times. This work investigates the strain through depth of uncycled and cycled samples using these coating techniques with synchrotron X-ray diffraction (XRD). In the TGO, room temperature XRD measurements indicated samples of both deposition methods showed similar in-plane compressive stresses after 300 and 600 thermal cycles. In-situ XRD measurements indicated similar high-temperature in-plane and out-of-plane stress in the TGO and no spallation after 600 thermal cycles for both coatings. Tensile in-plane residual stresses were found in the YSZ uncycled PS-PVD samples, similar to APS coatings. PS-PVD samples showed in most cases, higher compressive residual in-plane stress at the YSZ/TGO interface. These results provide valuable insight for optimizing the PS-PVD processing parameters to obtain strain compliance similar to that of EB-PVD. Additionally, external cooling methods used for thermal management in jet engine turbines were investigated. In this work, an additively manufactured lattice structure providing transpiration cooling holes is designed and residual strains are measured within an AM transpiration cooling sample using XRD. Strains within the lattice structure were found to have greater variation than that of the AM solid wall. These results provide valuable insight into the viability of implementing an AM lattice structure in turbine blades for the use of transpiration cooling.

”The man who views the world at 50 the same as he did at 20 has wasted 30 years of his life.”

–Muhammad Ali

”When you are talking, you are only repeating what you know; but if you listen, you can learn something new.” –Dalai Lama

ACKNOWLEDGMENTS

I'd like to firstly acknowledge and thank my advisor, Dr. Seetha Raghavan for her guidance and effort towards my professional development. Not many professors have the commitment to ensure the research of her students are of the highest quality.

Thank you to my collaborators: Dr. Bryan Harder (NASA), Dr. Vaishak Viswanathan (Praxair Surface Technologies), Dr. John Almer, Dr. Peter Kenesei, Dr. Jun-Sang Park (Argonne National Laboratory), and Dr. Marion Bartsch (DLR)

Thank you to my fellow student researchers such as Linda Rossmann, Brooke Sarley, Johnathan Hernandez, Zachary Stein, and Quentin Fouliard for your late night/early morning ANL songs, helpful discussions, and overall enthusiasm you bring to the work place. My Master's program was made more enjoyable because of each one of you.

Last bust most certainly not least, I would like to thank my family and friends for the support you've given me in the past two years. Deciding to go back to school was not an easy decision but was made a lot easier with the encouragement of those closest to me.

TABLE OF CONTENTS

LIST OF FIGURES

LIST OF TABLES

CHAPTER 1: INTRODUCTION

Higher turbine inlet temperatures (TIT) in gas turbine engines are consistently sought after to produce a high specific power output and overall engine efficiency according to the ideal Brayton cycle [7] shown in Equation1.1. The location of this section in a jet engine turbine is shown in Figure 1.1. Because of this increase in TIT, advanced material insulation and cooling methods are necessary to protect the turbine section components from the extreme environments that can exceed 1100 °C. The thermal management techniques of these systems, (shown in Figure 1.2) are comprised of thermal barrier coatings which use a roughly 250 μm thick layer of ceramic as thermal insulation along the outside wall of turbine blades and convective cooling on the interior and exterior of turbine blades via thin film. These are therefore appropriately named internal and external cooling [8, 9].

This work investigates the structural integrity of two methods of thermal management. Thermal barrier coatings (TBCs), with varying deposition techniques, are investigated during in-situ conditions at several points through their lifetime using synchrotron XRD. Using the same testing technique, residual strains of addivitively manufactured transpiration cooling holes are investigated and compared with additively manufactured solid material.

$$\eta = 1 - \frac{T_{compressorexit}}{T_{turbineinlet}} \tag{1.1}$$

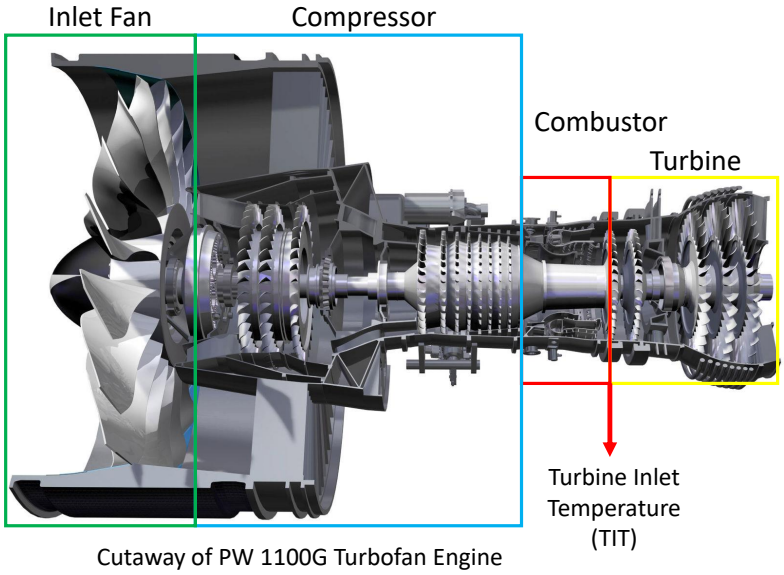

Figure 1.1: Typical jet engine schematic with location of turbine inlet temperature (TIT).

1.1 Deposition Methods for Thermal Barrier Coatings

Thermal barrier coatings (TBCs) have been used and improved upon since the 1970s and used commercially in the 1980s to increase the operating temperature of jet engine turbines and in effect, improve the efficiency of turbine engines [10]. With the use of TBCs temperatures can drop up to 300 °C from the top of the ceramic top coat to the underlying substrate, increasing the thermal resistance, durability, and lifetime of the blades.

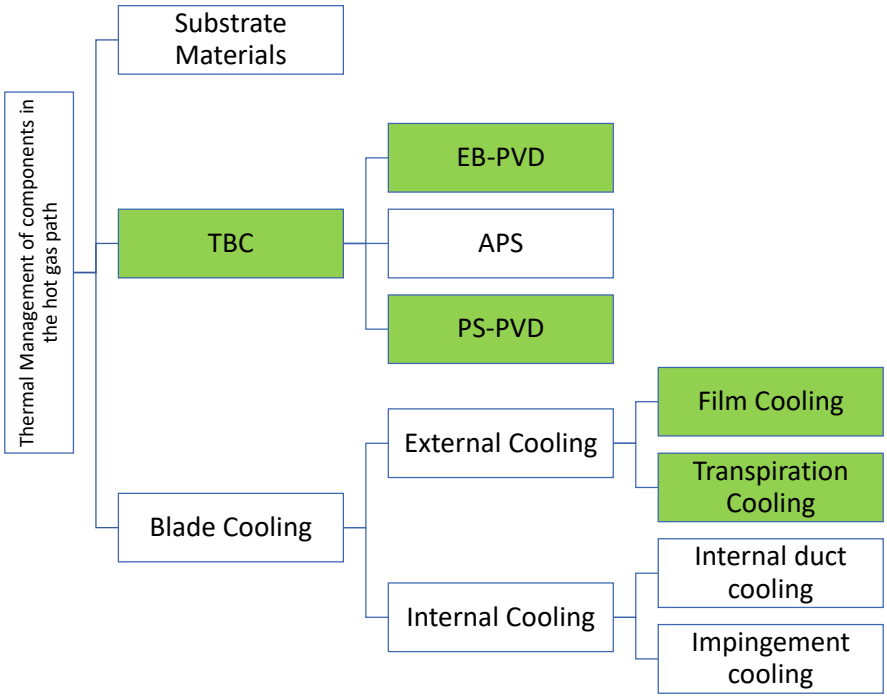

Figure 1.2: Flow chart of typical cooling methods for turbine section in aero-engines with the methods to be studied in this thesis highlighted in green.

Two deposition methods for TBCs are currently used in industry. Air Plasma Spray (APS), used primarily in power generation turbines, and electron-beam physical vapor deposition (EB-PVD), used more so in jet engine turbines. Plasma-spray physical vapor deposition is a newer deposition technique derived from the low pressure plasma spray (LPPS) deposition method. Originating in the 1990s, its customizable microstructure has been developed since, to be used as a deposition method for TBCs to replicate a similar columnar microstructure belonging to EB-PVD [11, 12, 13, 14, 15].

Another new and emerging deposition technique is solution precursor plasma spray (SPPS), where an aqueous precursor feedstock is injected into a plasma jet. The coating undergoes several physical and chemical processes before deposition which creates a strain tolerant, porous microstructure

with dense vertical cracks (DVC) that is also more resistant to corrosion than typical APS coatings due to increased coating density [16, 17, 18].

1.1.1 Background: Anatomy of TBC system

TBCs are a multilayered coating system as shown in Figure 1.3 typically composed of a nickel-based superalloy, which may be polycrystalline or single-crystal. Above this substrate is typically a metallic bond coat (BC), typically MCrAlY, platinum or nickel aluminides. The bond coat is used for adhesion to the yttria-stabilized zirconia (YSZ) ceramic top coat which provides the thermal insulation. The BC also provides oxidation protection for the substrate as an aluminum rich layer between the oxygen transparent top coat and the nickel-based superalloy substrate [19].

YSZ is often used for thermal barrier coating due to its low thermal conductivity at high temperatures (2.3 W $\cdot m^{-1} \cdot K^{-1}$ at 1000°), similar coefficient of thermal expansion (CTE) ($11 \times 10^{-6 \circ} C^{-1}$), and many oxygen vacancies [20, 19].

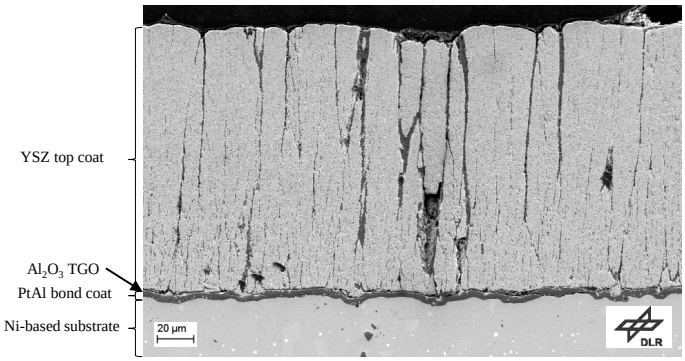

Figure 1.3: Scanning electron microscope (SEM) image of EB-PVD TBC with layers labeled.

The crystallographic phases of YSZ are the tetragonal (*t*), tetragonal prime (*t'*), tetragonal double prime (*t"*), monoclinic (*m*), and cubic (*c*) [21]. The *t'* phase is the most desired because of its high

tolerance to thermal shock and high bending strength, fracture toughness, and crack propagation energy [21, 22]. *t* is found most often in a TBC system after several heat treatments; however, upon cooling will transform to the undesired *m* phase which is accompanied by a 3-5% volume expansion [22]. This volume expansion places strain on the surrounding Zirconia, driving failure mechanisms such as cracking within the YSZ, delamination, and eventual spallation of the coating. A high cooling rate can repress this transformation from *t* to *m* [22, 21, 23, 24]. As the YSZ coatings decrease in yttria content, the transformation from *t* to *m* has been shown to increase with thermal cycling [25]. Differences in phases found in TBC systems can be found in Table 1.1. In EB-PVD coatings, as cycling increases, the microstructure can sinter, causing an increase in intercolumnar gaps and overall porosity in top coat. This makes the top-coat less strain tolerant and more thermally conductive which shortens the lifetime of the coating [19]. Surface roughness plays an important role as well in the lifetime of the coatings and aerodynamic efficiency of the turbine blades. Coatings with greater surface roughness can cause turbulent flow in the thin film of air from external cooling, increasing the temperatures experienced by the TBCs in the early stage turbine blades [26].

At high temperature, alumina (Al_2O_3) forms as a precipitate from the diffusion of aluminum from the BC and oxygen through the YSZ creating a thermally grown oxide (TGO) layer. This layer protects the bond coat from further oxidation after formation, preventing the spallation of the ceramic top coat from bond coat. Because it is formed at high temperatures, it is assumed to be in its stress-free state during operation. At room temperature, the TGO layer experiences large amounts of in-plane compressive stress and out-of-plane tensile stress. These interlayer residual stresses develop during cooling as a result of differences in CTEs between the substrate, BC, TGO, and YSZ which subsequently drive failure mechanisms including cracking, delamination, and spallation. CTE and oxygen diffusion differences between layers can be seen in Table 1.1. In the early stages of a TBCs lifetime ($\leq$ 10 thermal cycles), the compressive stress increases to its

maximum due to the initial growth of the TGO layer. After this maximum is reached, the TGO will be completely transformed to the metastable α phase and the compressive stress will begin to decrease slowly with respect to lifetime [27, 28, 29].

Table 1.1: Thermomechanical and Material Properties of materials used in TBC systems.

	7–8 wt. % YSZ (APS)	7–8 wt. % (EB-PVD)	7–8 wt. % (PS-PVD)	Al_2O_3	PtAl
Thermomechanical and Material Properties					
Coefficient of thermal expansion	11–13	11–13	-	7–10	14.6–16.1
($10^{-6}K^{-1}$)	[30, 31]	[32]		[32, 31, 33]	[34]
Oxygen diffusivity at 1000°C		10^{-11}		10^{-19}–10^{-21}	-
(m^2/s)		[30]		[30, 35]	
Material phases		*t'*, *t*, *c*+*m*		α	α
		[25]		[19]	[36]

The thermally grown oxide layer plays an important role in how a coating will fail and as a result, its overall lifetime. During thermal cycling, undulations will form at the TGO layer due to cyclic creep of the bond coat, causing points of high out-of-plane tensile stress concentration at the peaks and compressive stress at the troughs of the undulations which will lead to a mode 1 type fracture failure [29]. Compressive in-plane stresses form in between the peaks and troughs of the TGO layer and are typically correlated with the lifetime of the TBC system. [37] This roughening of the TGO layer, sometimes referred to as "ratcheting" is amplified with an as deposited rough bond coat and can cause cracking to transverse from crest to crest of the undulation, reducing the residual stresses found in the TGO layer [19, 29]. Finite-element modeling (FEM) has shown this same result that shows greater roughening of the TGO layer will cause greater reduction in residual stresses at this TGO layer [38]. With a low TGO roughness, cracks can form from thickness heterogeneities and cavity formations that expand parallel to the TGO layer due to shear forces, leading to a mode 2 type fracture failure [29, 19]. As the TGO layer fails compressive in-plane stress and tensile out-of-

plane stresses will be relieved due to delamination and spallation [39]. Once the top coat detaches from this layer, easier oxygen ingression into the bond coat and substrate will occur, resulting in an acceleration of futher TGO thickening [40].

1.1.2 Air Plasma Spray

Advancements in the 1970s led to the development of modern air plasma spray (APS) techniques in which the YSZ is applied by a powder feedstock injected into a plasma plume spraying over a large area with a high deposition rate. The deposited droplets solidify quickly and build up to create a highly porous coating with a rough top surface [2]. This high porosity creates a coating with very low thermal conductivity [19]. In addition to as-sprayed residual stress due to the rapid quenching of the sprayed layer, the APS method also results in a thick layer that is resistant to the elastic behavior of the underlying substrate during rotational load [41, 42].

APS coatings inherit microcracks during thermal cycling in directions both normal and parallel to the coating interface. Generally, more dense APS coatings have a higher thermal conductivity than porous APS coatings [43]; however, cracks normal to the heat flow reduce the thermal conductivity of the top coat whereas cracks parallel to the heat flux increase the overall thermal conductivity of the top coat [19]. Due to this variability in microstructural defects, APS coatings are used primarily in less physically and more thermally intensive applications such as fuel vaporizers and stator vanes [19].

Studies examining the stresses of APS top coats showed tensile stresses in their as deposited state [37]. Tensile stresses were found to be greater in depositions with lower deposition temperatures [44]. After thermal heat treatment APS samples have been shown to exhibit compressive stresses at the YSZ/TGO interface which trend towards zero at the free surface at the top of the YSZ layer. Higher stresses indicate greater adhesion between the YSZ and bond coat [37].

1.1.3 Electron-Beam Physical Vapor Deposition

As-sprayed intersplat cracking, CTE mismatch, and variable porosity were central to efforts to improve the APS coatings until electron-beam physical vapor deposition (EB-PVD) was introduced in the late 1980s[10]. EB-PVD produces an ultra-thin YSZ with a characteristic columnar microstructure normal to the BC surface that is both highly efficient for thermal protection and more strain-tolerant to the ductile behavior of the underlying substrate. Even though EB-PVD TBCs exhibit higher thermal conductivities (1.5 W/mK) than APS coatings (0.9 W/mK) [45, 46], this added benefit of high strain tolerance makes this coating method favorable for high pressure applications such as turbine blades. In the EB-PVD process, a ceramic ingot which in this work is 7–8$\%$ YSZ, is melted and subsequently evaporated using an electron-beam laser in a very low-pressure ($< 10^{-4}$ Torr or 0.13 Pa) chamber [2]. A horizontal actuator is used to move the substrate into the area of evaporation for the material to condense onto.

EB-PVD is a line-of-sight coating method meaning the back of the substrate will not be coated during deposition. This line-of-sight deposition prevents cooling holes from being clogged during coating but also requires the substrate rotate in the vacuum chamber to obtain an even coating. Additionally, lasers are used to heat the back of the substrate during deposition to ensure similar temperatures as the front of the substrate and, in turn, a similar deposition thickness and microstructure.

Additionally, EB-PVD coatings have a smoother surface than APS coatings, decreasing the overall heat transfer from the hot gas to the ceramic top coat. Lower top coat surface roughness is also beneficial for thin film cooling along the outer wall of the turbine blades as the flow will become more turbulent and increase overall heat transfer from the hot gas to the ceramic top coat [47].

Studies investigating the material and mechanical properties through depth of EB-PVD coatings

have been examined using both X-ray diffraction Raman spectroscopy [48].

1.1.4 Plasma-Spray Physical Vapor Deposition

High cost and long deposition time has spurred the development of a new coating, plasma-spray physical vapor deposition (PS-PVD). Modern efforts aim to implement the PS-PVD method, otherwise known as very low pressure plasma spray (VLPPS), to bridge the gap between APS and EB-PVD by creating unique microstructures with non-line-of-sight deposition capabilities, high deposition rate, and as a result low investment cost [2, 3, 49].

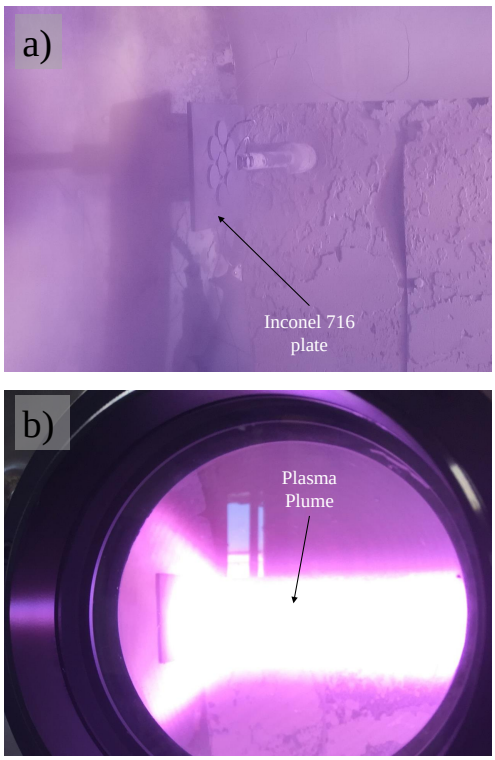

Figure 1.4: a) PS-PVD samples mounted on Inconel 716 plate in deposition chamber and b) Plasma plume depositing YSZ ceramic on René N5 substrates.

Through close control of a very low-pressure ($<$ 10 Torr or 1.3 kPa) environment, previous work

has shown that the same deposition chamber can be used to create conventional splat-like microstructures like APS through melting of the feedstock powders at higher deposition rates. Through vaporization of the powder particles at a lower deposition rate columnar microstructures similar to EB-PVD TBCs can be produced [50].

Due to this very low pressure, the plasma plume can be over 7 feet long and 3 feet in diameter while producing flow speeds between 2000 and 4000 m/s. Temperatures within the plasma plume can very between 6000 and 10000 K (10340 °F – 17540 °F) [2, 42]. While the plasma plume is much larger in this deposition method compared to APS, PS-PVD has a more uniform distribution of temperature and particle velocity. PS-PVD coatings can be applied rapidly due to the large size of the plasma plume without line-of-sight requirements, thereby allowing more complex geometries to be coated [2, 51, 52, 53]. Lowering chamber pressures increase the plasma diameter and length, better enveloping the target substrates. Increasing the power leads to higher plasma temperatures which in turn create thicker top coats [3]. Additionally, studies have shown top coat thicknesses, intercolumnar gaps, and porosity decreases in PS-PVD samples as deposition angle normal to the substrate is increased [3].

Residual early cycle stresses in the top coat of PS-PVD samples using Raman spectroscopy have shown these coatings to be in tension in the as deposited state and transition to compression between 25 and 100 thermal cycles [13, 54]. TGO roughnesses were seen to be a direct result of the bond coat surface roughness after deposition [13]. PS-PVD samples that experienced longer thermal cycling times (20 min) experienced a decrease in stress at the TGO layer [54]. This result differs from samples with less time at high temperature during thermal cycling (3 min) which showed an immediate increase in TGO residual stresses over thermal cyclings [13].

PS-PVD is also a promising coating method for applications such environmental barrier coatings, diffusion barrier layers, and electrically resistant coatings.

1.1.5 Motivation and Objectives for Investigation on TBCs

Here, we understand the similarities and differences of PS-PVD coatings and EB-PVD coatings using synchrotron X-ray diffraction (XRD) to evaluate the residual and cyclic lifetime stress behavior of the TGO and YSZ in these TBCs. In addition, the monoclinic phase volume fraction (mPVF) in the YSZ is investigated. Regardless of the deposition method, in-plane stress in the TGO has been shown to be a strong indicator of the overall life expectancy of the TBC [55, 56]. To determine the stress experienced by the TGO and YSZ within each coating system, 2D X-ray Debye patterns were collected in-situ during thermal cycles of as-deposited and thermally cycled coatings. Synchrotron XRD techniques have been developed to enable determination of the local orthogonal strain state of a specific phase within a complex system [57, 58, 37]. In this work, the diffraction strain of the α-Al_2O_3 and *t*-YSZ has been resolved into orthogonal stress according to the deviatoric deformation of the diffraction cone during thermal load [57, 59]. Additionally, mPVF calculations were conducted from synchrotron XRD scans and optical measurements using scanning electron microscopy (SEM) are used after thermal aging to provide a validation for the these operational behaviors found with 2D XRD.

1.2 Air Cooling Methods for Turbine Airfoils

Another area that was investigated in this work is the utilization of additive manufacturing to desing and manufacture transpiration cooling holes for external film cooling on turbine blades. Currently several methods of air cooling are used to prolong the lifetime and increase the durability of turbine blades. Internal cooling, in which the cool air is bled from the compressor and flows through the internal ducted chambers of the blade. Additional passageways on the interior of the blade are manufactured to increase the surface area of the interior wall exposed to the coolant flow which increases the heat transfer from the turbine blade wall. In addition to internal duct cooling,

impingement cooling is often use to further improve the heat transfer from the turbine wall to the coolant flow. This technique includes extrusions on the interior of the turbine blade wall to increase to surface area of the interior wall exposed to the coolant flow. The coolant flow that is used from internal cooling is then also guided along the outer wall with external cooling holes.

1.2.1 Discrete Cooling Holes

External cooling is comprised of two methods, discrete cooling and transpiration cooling, that use a boundary layer of air on the outer wall of the blades to create a layer of insulation between the hot air and the thermal barrier coating. For discrete cooling, holes are placed along the turbines that are cut through the entire outer wall of the blade. Different shaped holes with varying expansion rates are used for different sections of the turbine blade as a specific blowing ratio or film effectiveness is required for different surface geometries found on turbine blades. Additional information on the dimensions of some discrete cooling holes has been written by Bunker [60]

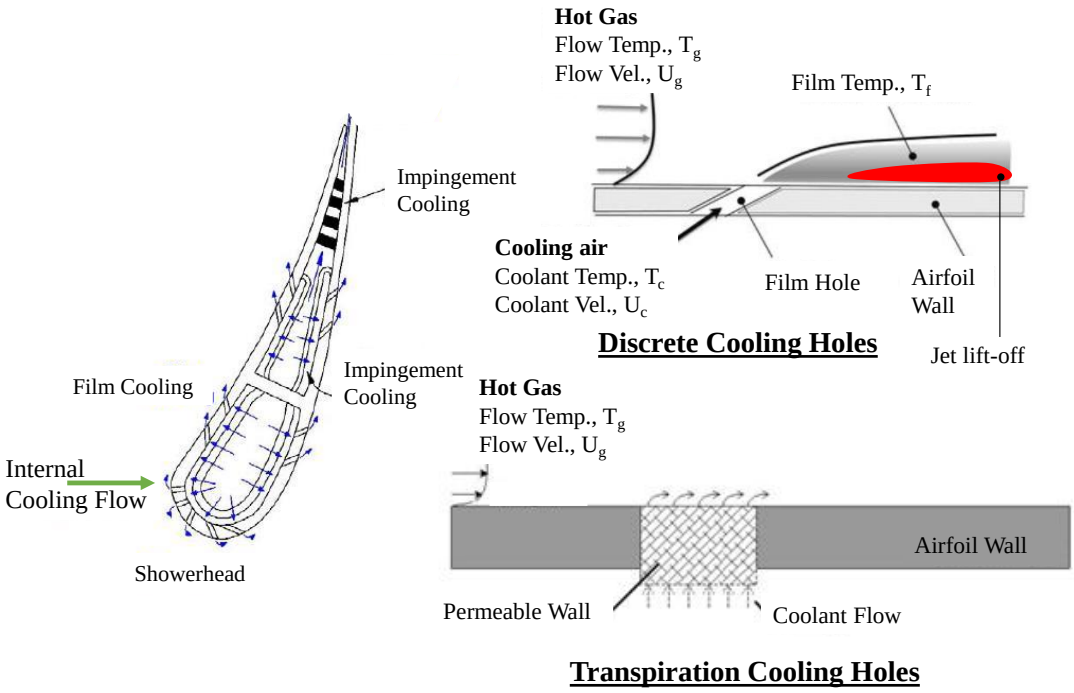

Figure 1.5: Diagram of discrete cooling with possible locations of failure and transpiration cooling porous media implemented in adiabatic wall.

1.2.2 Transpiration Cooling Holes

The second method used in external cooling is what is known as transpiration cooling. This method allows for a more uniform flow to exit the cooling holes and prevent what is known as jet-liftoff [61]. This phenomenon is the occurrence flow separation due to an increase or decrease in exit mass flow rate from the cooling holes. This flow separation then creates a pocket of hot air that is then directly exposed to the thermal barrier coating, increasing the average metal temperature and in turn lowering the lifetime of the blade due to creep failure [62].

Transpiration cooling has been implemented on turbine blades since the 1960s using a blade with metallic ribs on the exterior of the blade. Attached to these ribs is a porous sheet made of sintered gauze. The ribs support the structure and the sintered gauze creates the desired uniform flow that will bathe the exterior wall with low temperature cooling air [62].

Recent advancements in additive manufacturing has created an opening to rethink the design of transpiration cooling. Within the outer wall of the turbine blade a cavity is manufactured with an interior lattice structure to maintain the structural integrity of the blade. Cooling holes entering into and out of the cavity are used for the internal flow to then pass through the cavity, lattice structure, and second set of cooling holes, and subsequently on the exterior wall of the blade to create the desired air boundary layer [63]. Due to the complexity of this design, only additive manufacturing can be used to fabricate this structure. Both discrete cooling and transpiration cooling schamtics are shown in Figure 1.5. Additively manufactured transpiration cooling has also been investigated for other uses including combustion lining for gas turbine engines and rocket engines [64, 65].

1.2.3 Selective Laser Melting

Table 1.2: Chemical composition of Amdry 1718.

Chemical Composition (Amdry 1718)								
Element	Cr	Fe	Mo	Al	Nb+Ta	Ti	C	Ni
weight %	19	18	3	0.5	5.1	0.95	0.05	bal.

Selective laser melting (SLM) is a method of additive manufacturing that can be used for materials with a high melting temperature such as nickel based superalloys used in jet engine turbines. Within the deposition chamber are three sections. The first section in the container where the ma-

terial powder (0.1 mm thick) is stored and then fed to the second section, the build platform. The powder is fed evenly onto the platform via a powder leveling roller (part 3). Excess powder fed onto the build platform fills the third section, the recycling area. Powder that isn't melted during deposition can be recycled and used in a limited amount of future SLM processes. Once the powder is placed on the build platform, a high-energy laser beam, part 4, is directed onto the deposited layer via mirrors and melted to form a solid body. When a layer is finished, the build platform lowers and a new bed of powder is spread on the build platform. The deposition chamber takes place in an argon or nitrogen rich atmosphere to minimize oxidation during the deposition process. This process is shown in Figure 1.6.

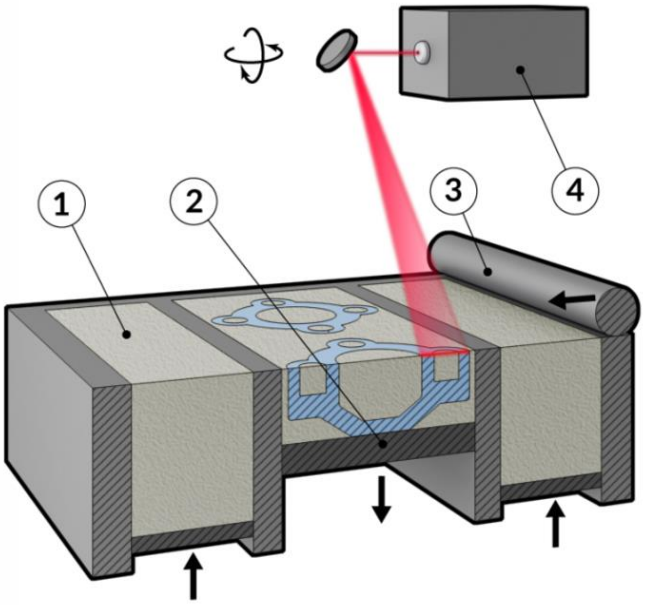

Figure 1.6: Schematic of SLM process and parts required for deposition.

During the SLM process the printed material is heated above its melting temperature. This process is very fast due to the small size of the source of heating that creates a melt pool that is relatively

small compared to the build platform. Due to this iterative process of heating and cooling during deposition the surrounding material, in what is known as the heat-affected zone (HAZ), experiences repeated heat exposures as more material is deposited. This repeated heating process of the material in the HAZ is referred to as ”intrinsic heat treatment” [66].

1.2.4 Motivation and Objectives for Investigation of T-cooling

Because of intrinsic heat treatment, residual strain within the material can vary along the build direction. In addition, strains may vary in complex geometrical builds compared to solid bulk material. These residual strains are important in understanding the thermal and mechanical limitations of SLM additively manufactured parts to be used in jet engines with transpiration cooling lattice structures. Using synchrotron XRD, strains perpendicular and parallel to the build direction can be found after deposition and during operational conditions. This work provides an initial effort consisting of the design work for samples to be tested in operational conditions and experimental work consisting of two directional residual strains in an additively manufactured Amdry 1718 sample perpendicular to the build direction with a novel transpiration cooling lattice structure using synchrotron XRD.

CHAPTER 2: SAMPLE MANUFACTURING

This chapter begins with the manufacturing of both PS-PVD and EB-PVD thermal barrier coatings. Thermal cycling and post processing of these samples for synchrotron XRD measurements are discussed. After this, a design study on additively manufactured transpiration and discrete film cooling hole samples is discussed along with the manufacturing of an existing transpiration cooling sample that was used for preliminary synchrotron XRD residual strain measurements.

2.1 Thermal Barrier Coatings

Samples were manufactured by EB-PVD and PS-PVD techniques. Of these, 8 EB-PVD and 12 PS-PVD samples were studied using synchrotron XRD. A full description of the samples used is shown in Table 2.3. The Ni-based superalloy substrates for all samples were René N5 discs 25.4 mm in diameter and 3 mm thick. Chemical composition of the subtrates are shown in Table 2.1. A platinum aluminide (PtAl) bond coat was applied to all samples by Praxair Technologies. The bond coat had an average thickness of 52 μm measured using the average of two micrometer measurements halfway between the center and edge of the discs before and after deposition. Samples with both PS-PVD and EB-PVD deposition method were coated with 7–8 $\%$ yttria-stabilized zirconia (YSZ); typically used on turbine blades due to its low density, high hardness, melting temperature, and resistance to corrosion [19].

Table 2.1: Chemical composition of René N5.

Chemical Composition (René N5)									
Element	Co	Cr	Al	Ta	W	Re	Mo	Hf	Ni
weight %	8	7	6.2	6	5	3	2	0.2	bal.

2.1.1 PS-PVD Coatings

The PS-PVD samples were coated at NASA Glenn Research Center in five separate batches with 7 samples coated in each batch. The samples were spot welded to an Inconel 716 plate in a hexagonal pattern with k-type thermocouples placed above and below the center sample as shown in Figure 2.1a.

Table 2.2: Processing parameters used for PS-PVD technique. Similar processing parameters have been used to fabricate TBC's with columnar microstructures similar to EB-PVD [2, 3, 4].

PS-PVD Processing Parameters						
Deposition Temperature (°C)	Current (Amperes)	Power (kW)	Chamber Pressure (torr)	Standoff distance (meters)	Ar/He ratio	Total Plasma Gas (NLPM)
800-850	1800	80	0.785	1.65	1:2	80

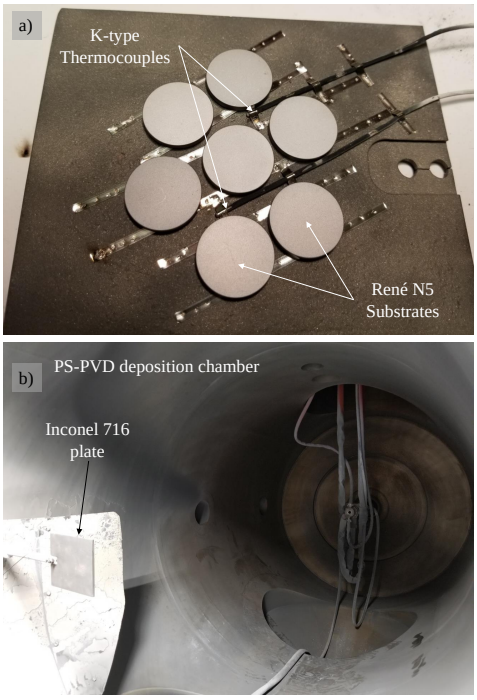

Figure 2.1: a) PS-PVD samples mounted on Inconel 716 plate and b) Plate mounted in PS-PVD chamber.

The deposition chamber, with the plate mounted inside as shown in Figure 2.1b, was then pumped to 0.1 Torr (13 Pa) and left for at least one hour to reduce humidity. The chamber was then back-filled with an argonne-helium ratio shown in Table 2.2 to a chamber pressure of 30 Torr (4 kPa). Following the addition of the Ar:He mixture, the plasma torch was lit and the chamber pressure was reduced to about 1 Torr (133 Pa). The plasma plume contained the yttria and zirconia powders fed through two feedstocks and impinged on the mounting plate for 26–30 minutes at a temperature range shown in Table 2.2.

Each sample coated in its respective batch was given a cycling lifetime of 0, 100, 200, 300, 400, and 600. Due to time constraints, only four batches of samples given 0, 300, and 600 thermal cycles were studied using synchrotron XRD as shown in Table 2.3.

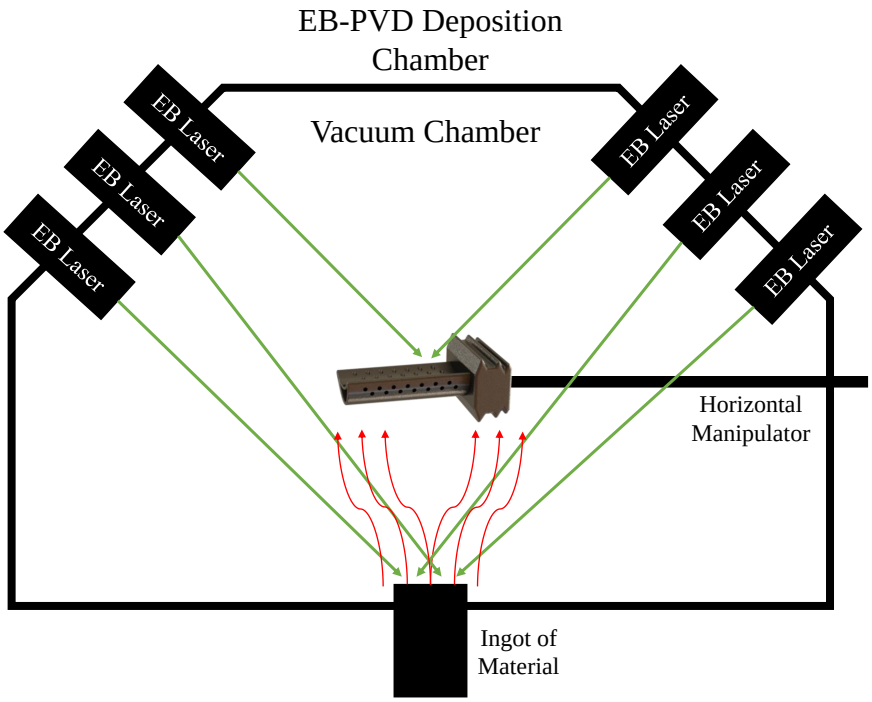

Figure 2.2: Schematic of EB-PVD deposition process.

The target thickness for each sample's top coat was 200 μm. Average YSZ thicknesses after deposition are shown in Table 2.3. The PS-PVD coatings had a slightly lower mean thickness (217.6 $\pm$ 35 μm) than EB-PVD coatings (218.6 $\pm$ 26 μm). This greater standard deviation in PS-PVD samples can be attributed to the process variability between runs for PS-PVD. Top coat thickness was determined by measuring each sample's thickness with a micrometer before and after deposition; in each case two measurements halfway between the center and edge of the disc samples were averaged.

2.1.2 EB-PVD Coatings

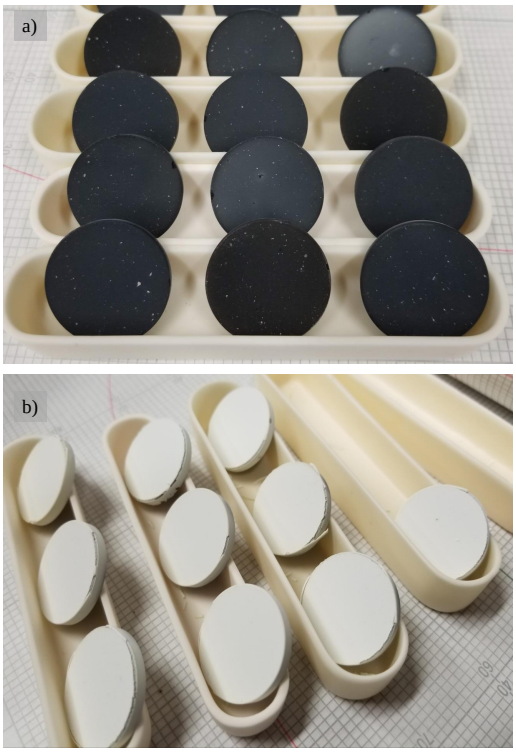

Figure 2.3: a) PS-PVD samples before and b) after 1-hour heat treatment in ceramic boats.

EB-PVD samples were coated with a 7–8% YSZ layer on top of the PtAl bond coat applied. All nine EB-PVD samples were manufactured by Praxair Coating Technologies in a single batch. A schematic of EB-PVD deposition chamber is shown in Figure 2.2. EB-PVD samples' bond coats were not measured so it was assumed the mean bond coat thickness was the same as the measured mean thicknesses of PS-PVD samples.

2.1.3 Cyclic Thermal Aging and Sample Slicing

Table 2.3: Sample count and average thickness for all experimental samples. *PS-PVD samples were given a 1-hour heat treatment at 1100°C to achieve stoichiometry.

Deposition Technique	Number of Samples			Average Top Coat Thickness (μm)
Number of Thermal Cycles	0*	300	600	
EB-PVD	3	2	3	219 ± 23
PS-PVD	4	4	4	222 ± 26

The PS-PVD samples were given a 1-hour heat treatment at 1100 °C with a 5 °C/min. ramp up and ramp down rate to achieve stoichiometry, as they are oxygen-deficient in their as-coated state. This is evident by their black color after deposition as seen in Figure 2.3a. Figure 2.3b shows the samples after the conversion from ZrO to ZrO_2 during heat treatment. This heat treatment also served to develop a TGO in the samples. After deposition, roughness measurements were completed for both PS-PVD and EB-PVD samples using Zygo NewView 7200 profilometer. PS-PVD samples had a greater surface roughness (9.3 ± 0.6 μm) than EB-PVD samples (2.1 ± 0.4 μm). The large difference in YSZ thickness shown in Figure 2.4 could be due to the location of which the SEM images were taken. PS-PVD thicknesses may fluctuate depending on location within the plasma plume because of the processing variances [49].

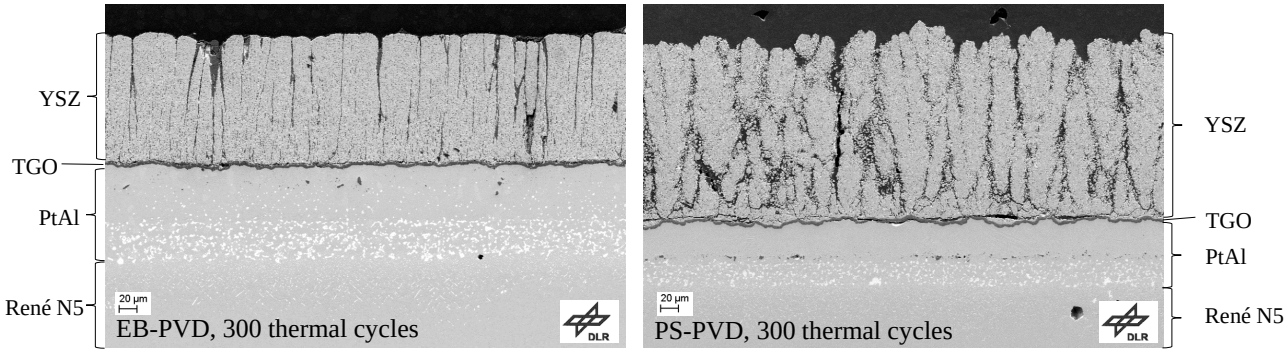

Figure 2.4: SEM image of both EB-PVD and PS-PVD techniques after 300 thermal cycles [1].

A number of the EB-PVD and PS-PVD samples were thermally cycled as summarized in Table 2.3. Two samples from each deposition batch of PS-PVD samples were put aside after heat treatment to compare to uncycled EB-PVD samples. Cycling was done in an open-air furnace with a hot time of 1 h at 1100 °C and a ten minute cool time with fan-assisted cooling during which the temperature reached 200 °C.

All samples were prepared to optimize X-ray transmission and minimize stress-relieving effects of cutting [37]. A center section (width = 2.5 mm) were cut from coated, thermally cycled buttons with 25.4 mm diameter using a diamond saw. The samples were then rinsed with cold water and dried with compressed air. No spallation was visible after cutting. The remaining sections of the TBC samples were kept for SEM and EDS measurements. The results of this work is shown in other work [1].

2.2 SLM of Cooling holes

Table 2.4: Chemical composition of Inconel 718.

Chemical Composition (Inconel 718)									
Element	Ni	Cr	Nb+Ta	Mo	Ti	Al	Co	C	Fe
weight %	50-55	17-21	4.75-5.5	2.8-3.3	0.65-1.15	0.2-0.8	1	0.08	bal.

A mock leading edge segment of a turbine blade was designed at UCF and manufactured with the intent to test for heat transfer results [63]. This sample is shown in Figure 2.5. Using Amdry 1718 material which has a similar chemical composition as Iconel 718 but with a smaller particle size, the sample was fabricated using the SLM AM process [67]. Effects of particle size on mechanical properties such as creep, tensile strength, and crack growth have been studied for Inconel 718. [68] A chemical composition of Amdry 1718 can be seen in Table 1.2. The lattice structure within the outer wall is a novel design that allows for an open passage for the coolant flow to move along the lattice structure and out along the outside wall. After deposition the sample was heat treated to 950 °C for two hours and cooled to room temperature at a rate of 10 °C/min.

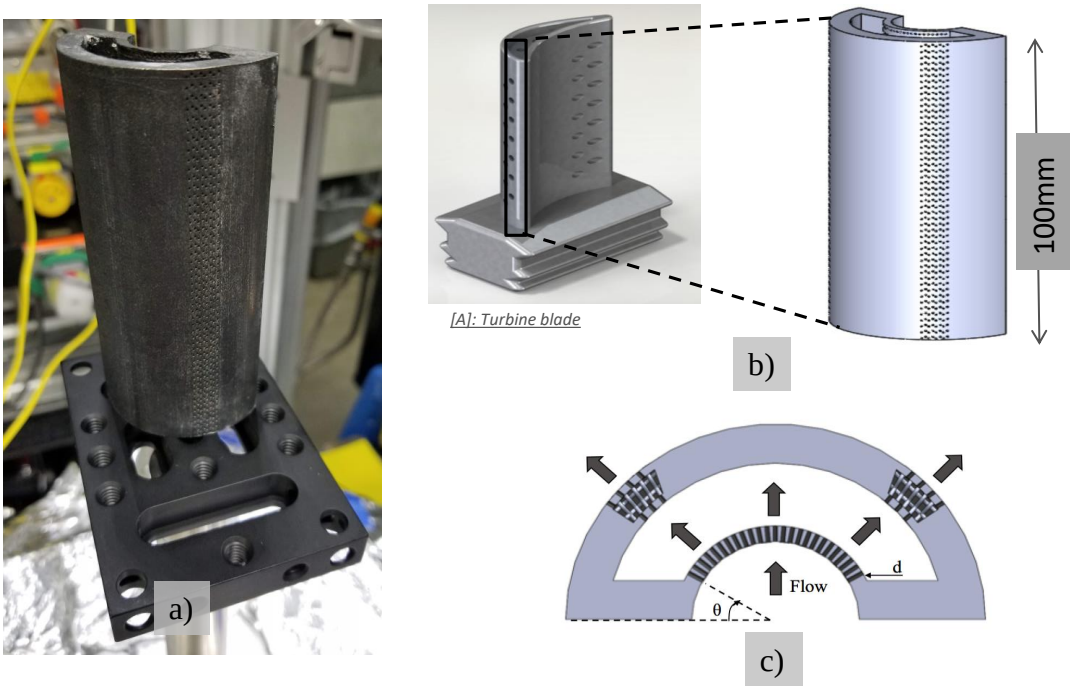

Figure 2.5: Amdry 1718 transpiration cooling sample a) mounted in synchrotron XRD hutch b) in CAD with representation of section to replace in turbine blade and c) cross section view.

The diameter of the laser beam was approximately 70 μm. Each layer thickness was 30 μm and the powder grain size was between 25 & 45 μm. The designed diameter of holes in the impingement array and porosity of the cavities are 0.5mm and 57 % respectively [63, 67]. The lattice is an arrangement of intertwined material with diameters of 0.5 mm. The structure build angle is 60 ° with respect to the build plate to disregard support that would otherwise be needed.

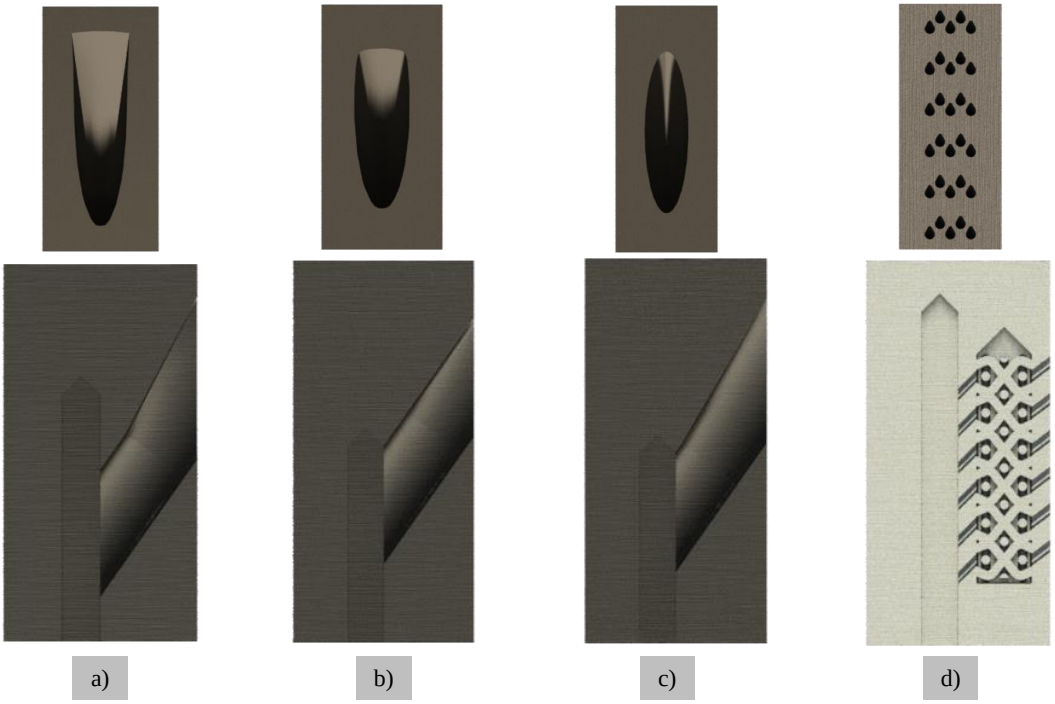

Figure 2.6: Cross sectional and top down views of discrete cooling hole type a) A b) B c) C and d) transpiration cooling holes.

Along with this mock leading edge segment sample, several samples were manufactured for future synchrotron XRD studies using Inconel 718. The chemical composition of Inconel 718 can be seen in Table 2.4. The samples were manufactured with the intent of conducting in-situ experiments where air flow is pushed through the cooling holes while the exterior is heat up to 750 °C. This temperature was chosen to avoid the changes in strain from Inconel 718's phase change at 800 + °C [69].

Samples manufactured with transpiration and discrete cooling holes were printed vertically as shown in Figure 2.7 and in one batch. Each sample had a rectangular flow channel for the coolant air to move along and then through the film cooling hole. Notice in Figure 2.7 that two walls

angled at 45° were placed at the top of the interior flow channel. This was designed because of the SLM process; an overhang angle less than 45° with respect to the build plate will result in the material collapsing in on itself [70]. Additionally, the lattice structure inside the cavity is designed to keep the entrance and exit holes open for air to flow through as seen in Figure 2.6a.

Additionally, samples with discrete hole designs were manufactured. Sample A, otherwise known as "diffused trapezoidal shaped hole" expands both laterally and longitudinally and has shown very little to no flow separation at the exit of the cooling hole and higher film effectiveness in low and moderate blowing ratios [71]. This discrete cooling hole design is most commonly used in industry because of both its performance and manufacturing simplicity. Sample B, also a "diffused trapezoidal shaped hole", expanding laterally with filleted corners and showed a consistent flow effectiveness irrespective of blowing ratio [72, 73]. Sample C utilizes an elliptical cooling hole shape which expands along the semi-major axis of the ellipse. This discrete cooling, along with cooling hole type B, has been studied in stagnation showerhead region of the turbine airfoil and shown a 10–20 % increased averaged effectiveness [74].

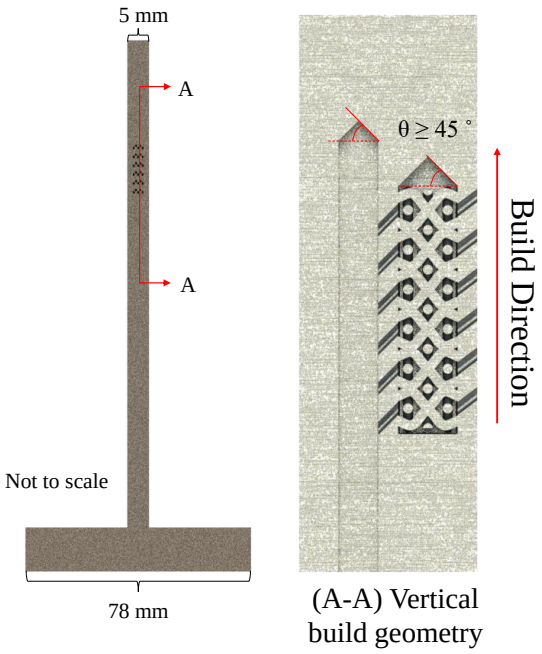

Figure 2.7: Transpiration cooling sample design with cross-section of flow channel and internal lattice structure.

CHAPTER 3: IN-SITU X-RAY DIFFRACTION MEASUREMENTS OF STRAIN AND PHASE VOLUME FRACTION

In this chapter the method and theory behind X-ray diffraction is explained, followed by relevant studies on TBCs and the reasoning behind XRD parameters chosen. Relevant studies and reasoning for parameters chosen for the AM transpiration cooling study is then elaborated upon after. Synchrotron X-ray diffraction experimental procedures are then described for the TBC investigation, followed by the transpiration cooling investigation. Lastly, the analytical procedure is described for the TBC investigation and transpiration cooling investigation.

3.1 X-ray diffraction

X-ray diffraction is a testing method used to study the inter-atomic distance of lattice planes found in a crystalline material. In this process an X-ray, or high energy monochromatic light with a wavelength, λ, probes atoms in a crystalline material. Because of the connection between an X-ray's wavelength and the atomic spacing of material the X-ray will reflect at a certain angle, 2θ, through an interference effect called diffraction. This relationship is known as Bragg's Law as shown in Equation 3.1.

$$n\lambda = 2d_{hkl}sin(\theta) \tag{3.1}$$

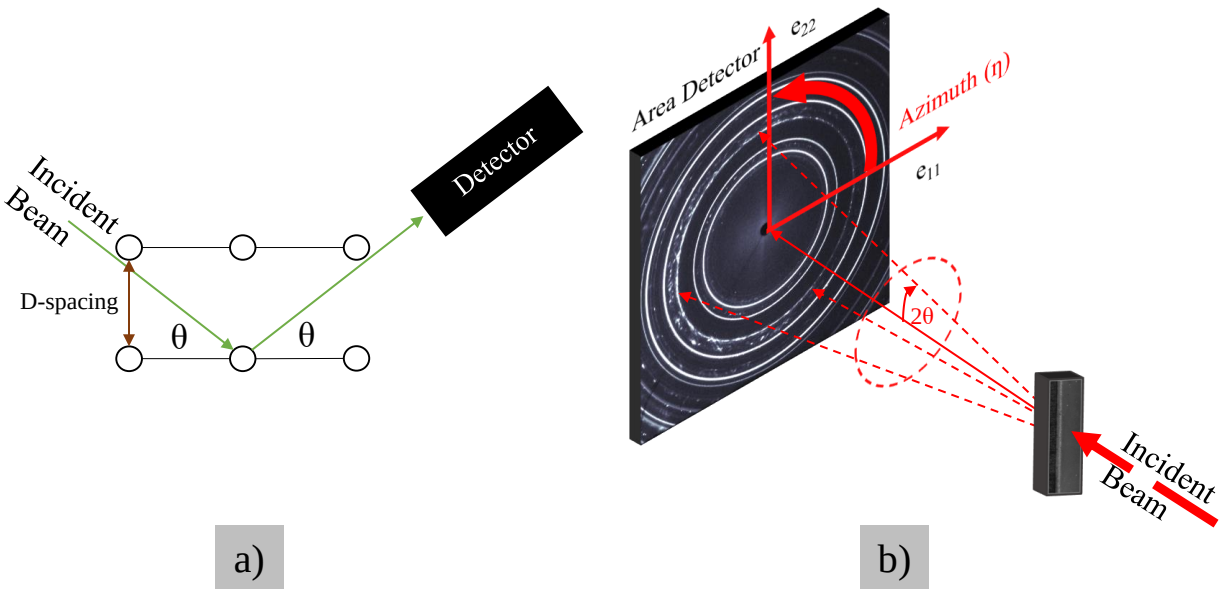

Figure 3.1: Schematic of X-ray diffraction experimentation for a) 1D XRD and b) 2D XRD.

The arrangement of atoms are defined by the unit cells with which the atoms occupy. These unit cells are stacked continuously on top of one another, causing a periodic arrangement of the atoms. The unit cell dimensions are defined by its edge lengths (a, b, and c) and angles with respect to its origin (α, β, and γ). The connection between these atoms are called lattice planes, which are periodic in nature just like the unit cells in which they stay and the distance between these lattice planes is known as d-spacing. The orientation of these lattice planes are represented by Miller indices (h,k,l); vectors normal to the unit cell's origin. Because of the Bragg's Law relationship, exiting a material with an X-ray of a constant wavelength, λ, while recording the intensities of the X-ray diffracted at a given angle, 2θ, the atomic plane spacing can be calculated. When material experiences stress, the d-spacing between lattice planes will increase or decrease. Given the d-spacing for the material in the stress free state and the measured values of d-spacing

during experimentation, the strain within a material can be determined.

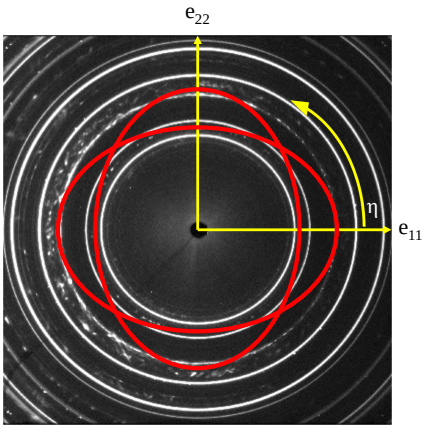

Figure 3.2: 2D XRD projected rings distorting to ellipses due to stress in the e11 or e22 direction. Blue lines indicate rings sectioned for analysis.

Using a high energy X-ray provided by a synchrotron particle accelerator, the X-ray and its diffracted beams can pass through a polycrystalline material, diffracting the X-ray in 360 ° about the incident beam axis to produce Debye-Scherrer rings onto an area detector in what is known as transmissive or 2D X-ray diffraction due to it's ability to measure strain in two directions. This is different from 1D X-ray diffraction where only the reflected X-ray intensity will be measured with the detector moving in an angular motion opposite of the X-ray source. This produces overall d-spacing and strain measurements, making it less advantageous than 2D XRD. Additionally, the use of a high energy X-ray and 2D area detector can be used to shorten measurement times, allowing for in-situ conditions to be applied during measurements. A schematic of the two X-ray diffraction methods is shown in Figure 3.1.

In 2D X-ray diffraction, when lattice planes orientated in the e11 direction shown in Figure 3.1

experience stress, d-spacing will increase or decrease. This will cause the concentric circle appearing on the area detector to distort into an ellipse with the major axis in the e11 direction shown in Figure 3.2. The same will occur in the e22 direction when lattice planes orientated in that direction become stressed. An illustration of this change can be seen in Figure 3.2. Additionally, phase volume fraction (PVF) can be calculated using the integrated intensity of material phase specific lattice planes of a material around the azimuth, η [75]. Several very good textbooks are recommended for a general and in-depth introduction to 2D XRD [76, 59].

The Advanced Photon Source at the Argonne National Laboratory provides the necessary extremely bright and high energy X-rays used for 2D XRD. This facility uses a linear accelerator and bending magnets to produce and direct a stream of electrons into a storage ring which spans 1,104 meters in circumference. This ring diverts the high energy X-rays to 40 hutches constructed around the storage ring. The experiments in this work were conducted at the first beamline (1-ID) in the path of the accelerated electrons, making it the optimal sector of the APS facility to measure large volume and highly dense material. The resulting beam travels through a monochromator followed by silicon refractive lenses to adjust the energy levels of and focus the beam respectively. The square panel 2D area detector used for these experiments, dimensioned 410 x 410 mm, had a pixel size of 200 μm. The detector's high resolution, collection speed, and signal-to-noise ratio makes it ideal for strain measurements.

3.2 2-D X-ray Diffraction Studies on TBCs

As mentioned previously, polycrystalline material provide Debye-Scherrer rings used for two-directional strain measurements. Incomplete rings which can result from textured materials require assumptions in the fitting process which create a less reliable strain result in directions of missing intensities. To account for this anisotropy which is found in the top coat of TBCs deposited using

the EB-PVD coating method, the beam window must include many grain orientations of the YSZ top coat. Creating a large length of the beam window (300 μm) in the direction parallel to the top coat interface and smaller length in the orthogonal direction, enough grain orientations can be captured to obtain the required full Debye-Scherrer rings without diminishing the benefits of high spatial resolution (30 μm) through the coating. Additionally, 30 microns was chosen to fully capture all strains in an undulated TGO of the TBCs as a typical TGO thickness can range between 1-10 μm [19]. The results presented in this work show both in-plane (e_{22}) and out-of-plane (e_{11}) strains through depth of the TBC system.

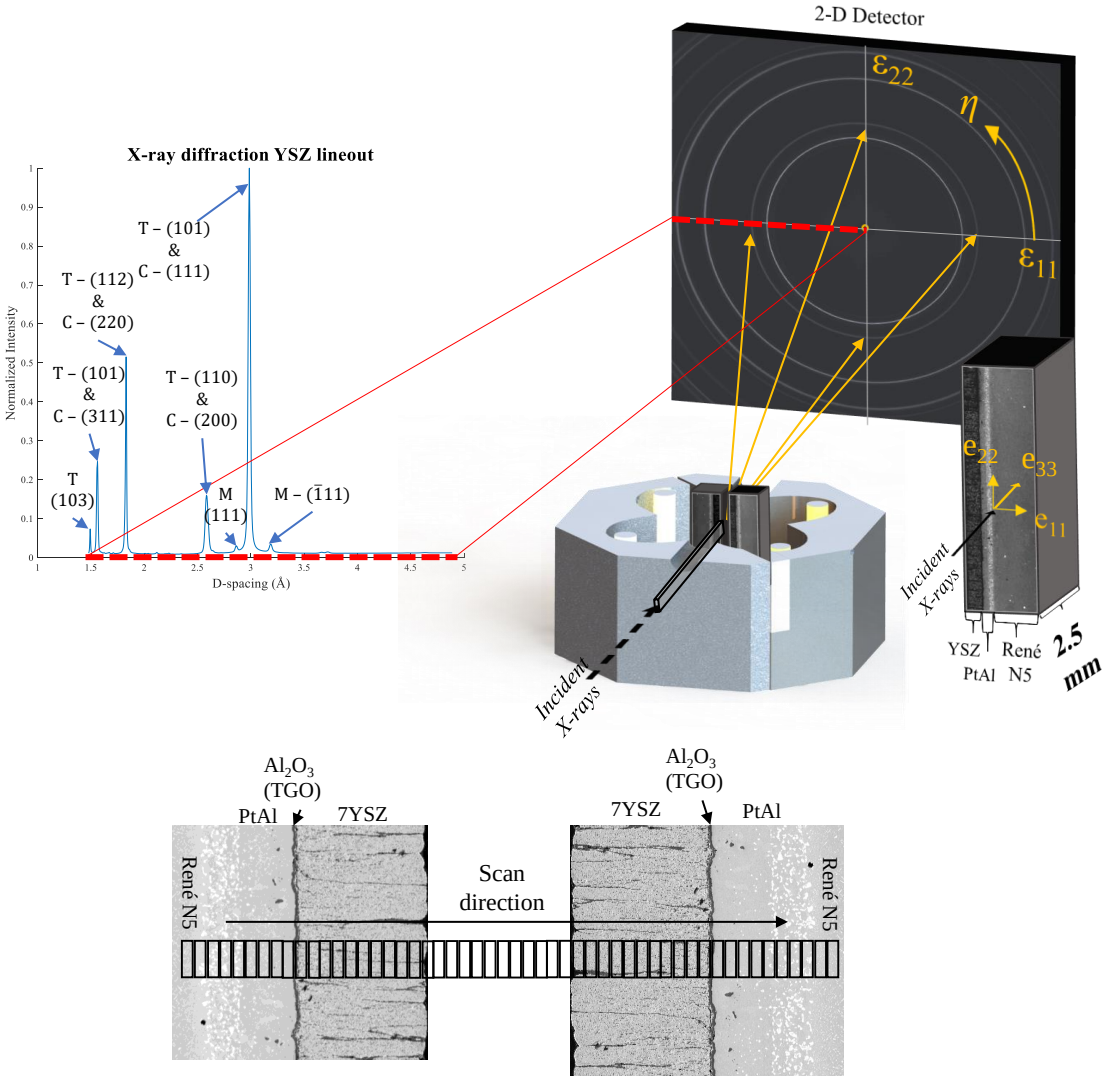

Figure 3.3: Schematic of synchrotron X-ray diffraction experimentation with measurement points throughout the coatings.

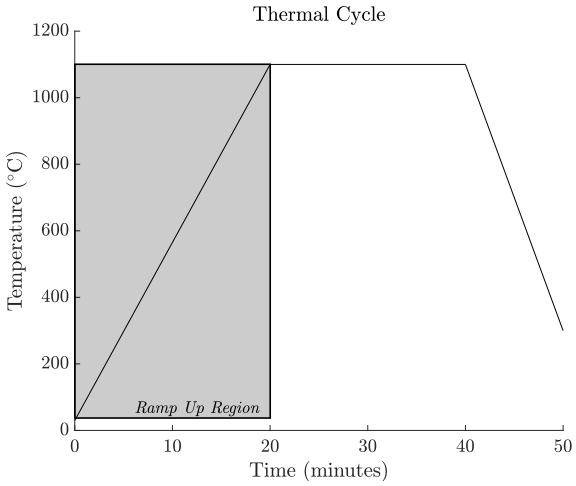

Figure 3.4: One thermal cycle performed during in-situ X-ray diffraction experiments.

TBCs experience the extreme operating temperatures found in turbine sections of aero engines (1000–1300 °C after air film cooling) [77, 78]. To apply these temperatures, the TBCs were place in an E4 infrared heater with an entrance and exit hole during experimentation for direct and diffracted beam respectively. A sample holder was manufactured to hold two samples simultaneously with a K-type thermocouple contacting the top surface of the TBCs. The X-ray energy used in these experiments was 71.676 keV with a 0.172 wavelength. Sample to detector distance was 1697.5 mm. A CeO_2 powder specimen was used for calibration of the area detector. Previous studies have used this experimental setup to successfully capture in-situ strains within TBCs[79, 80, 81, 82, 83].

During thermal cycling, the sample was moved continuously along the e_{11} direction while acquiring diffraction patterns using the area detector through the YSZ and in the TGO. The heater ramped up for 20 minutes at a rate of 55 °C/min and then held at high temperature (1100 °C) for 20 minutes. The heater's power was then set to zero and the samples cooling to around 300 °C in 10 minutes. The measurements were then stopped and the samples were cooled back down to room temperature through fan cooling. An illustration of this temperature profile that samples

experienced during experiments is shown in Figure 3.4.

3.3 2-D X-ray Diffraction Studies on Additively Manufactured Metallics

High-energy synchrotron X-ray diffraction is a great experimental technique used to measure a high-resolution strain in materials. The 1-ID beamline at the Advanced Photon Source (APS) at the Argonne National Laboratory (ANL) in Chicago, IL is used to specifically measure the strain in the nickel based superalloys because of ability to penetrate dense metals due to its high energy.

Several factors when determining the experimental parameters are taken into consideration. Materials additively manufactured using SLM have a typical microstructure that forms long needle like grain orientations in the build direction. To measure strain in multiple directions (e11 & e22) a complete Debye-scherrer ring on the 2D detector is desired. In order to get this desired full ring, the X-ray beam window was configured to 200 μm x 200 μm. This beam window captures enough grain orientations to obtain a complete Debye-scherrer ring but also increases the overall intensity of the incident beam, allowing for a larger probed volume. The different beam windows overlayed on a scanning electron microscope image (SEM) of inconel 718 SLM sample manufactured in 2016 at DLR shows the importance of beam window dimensions and the resulting Debye-sherrer rings. Notice in Figure 3.5a the beam window captures only a few of the grain orientations, resulting in an textured ring. This texturing requires estimation and is much less preferred to the complete rings shown in Figure 3.5b.

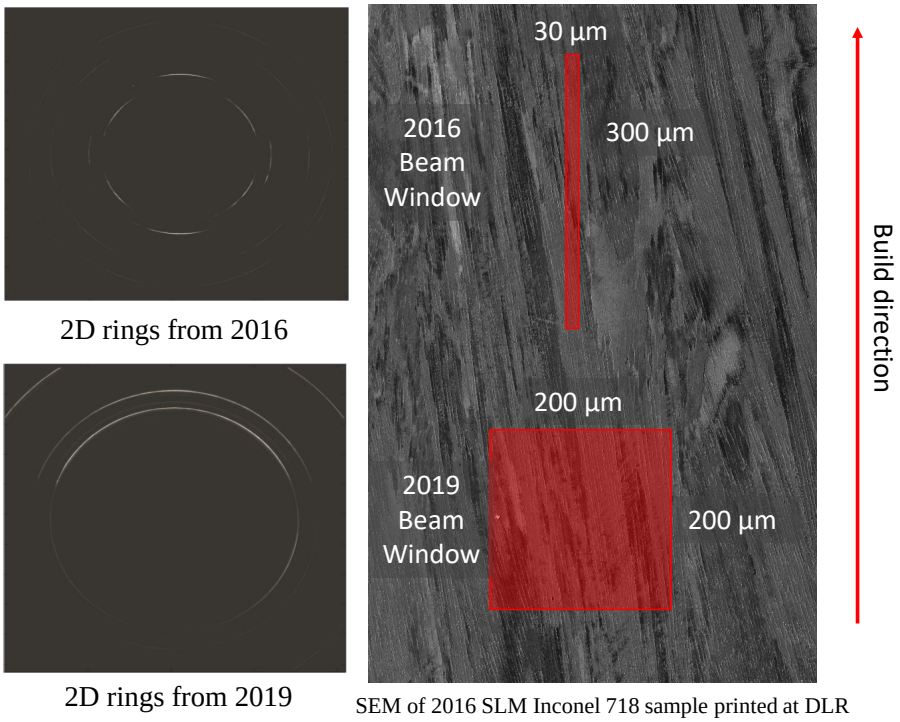

Figure 3.5: Beam window used in 2017 and 2019 ANL experiments on SLM samples along with their resulting Debye-scherrer rings.

3.4 2-D X-ray Diffraction Experimental Procedure

3.4.1 2-D XRD Experimental Procedure for TBC measurements

For the PS-PVD and EB-PVD experiments, a sample holder was manufactured to hold two samples with a K-type thermocouple contacting the top surface of both TBCs. The samples were mounted inside an infrared heater that included entrance and exit holes for beam access and diffraction measurements.[82, 83] A picture of the experimental setup is shown in Figure 3.6. During thermal

cycling, the samples were moved horizontally with respect to the beam. This allowed for measurements to be taken through depth of the YSZ, TGO, bond coat, and substrate. The sample to detector distance, beam center, and detector tilt was calibrated with ceria powder before experimentation in the same sample holder used for in-situ measurements. For each sample, measurements were taken during a single thermal cycle using a beam window size of 30 x 300 μm^2 and beam energy of 71.68 keV. In order to remove residual background measurements, dark files were collected while the beam shutter was closed before each set of experiments.

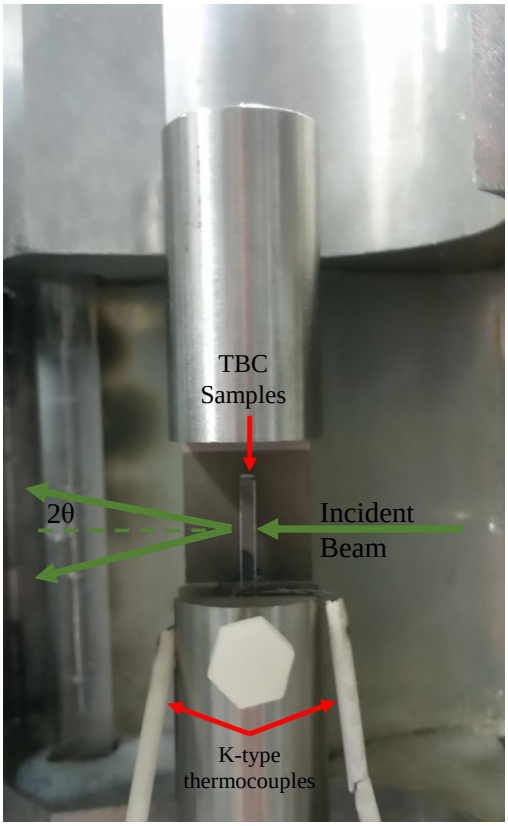

Figure 3.6: Photo of sample holder with two TBC samples mounted. Two loop style K-type thermocouples attached to the YSZ face of both samples.

The thermal cycle began at room temperature and increased at a rate of 55 °C/min until the maximum temperature of 1100 °C was reached, then held for 20 minutes. The heater was then shut off

and XRD measurements continued during cool-down until the sample temperature reached 300 °C, at which point measurements were stopped so insulation could be removed and the heater opened for faster cooling to room temperature. Each measurement extended from the substrate of the left-hand sample across the TBC thickness, air gap, and second TBC thickness, with a step size of 30 μm until the substrate of the right-hand sample was reached.

3.4.2 2-D XRD Experimental Procedure for T-cooling measurements

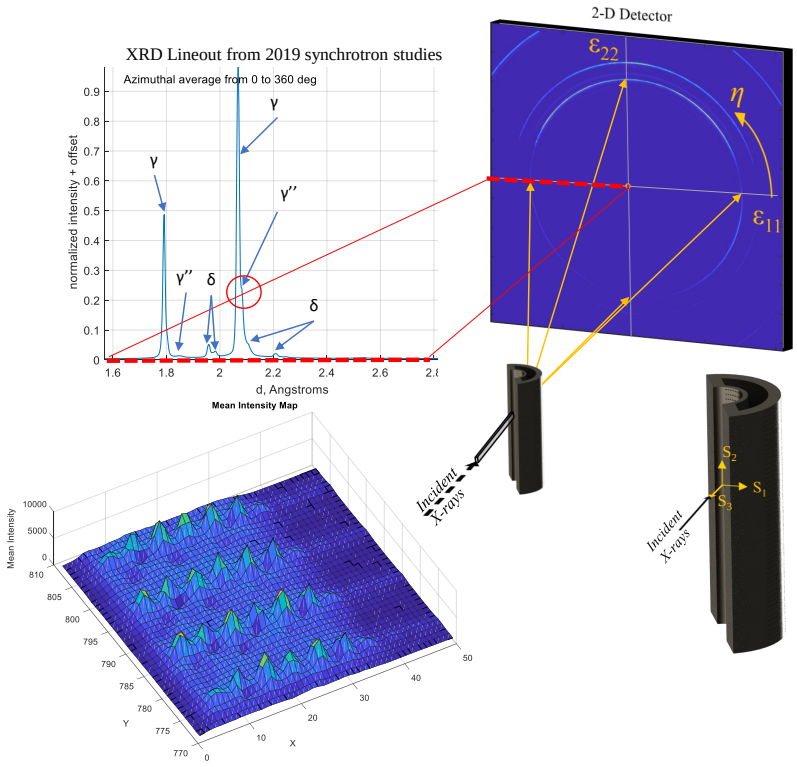

Figure 3.7: 2019 XRD setup with resulting 2D detector projections, averaged XRD lineout, and mean intensity map of the scan.

The transpiration cooling sample was orientated during experimentation to obtain measurements through the outer wall containing the lattice structure as shown in configuration 1 of Figure 3.8.

An schematic of the experimental setup and corresponding Debye-Scherrer rings, averaged XRD lineouts, and mean intensity map from scans is shown in Figure 3.7. Experiments measuring the two-directional strain in the solid AM outer wall were also taken. Sample orientation of this experiment is shown in configuration 2 of Figure 3.8. Measurements were taken in a 10 mm x 8 mm map the e_{11} and e_{22} direction respectively with a step size of 200 μm in both directions.

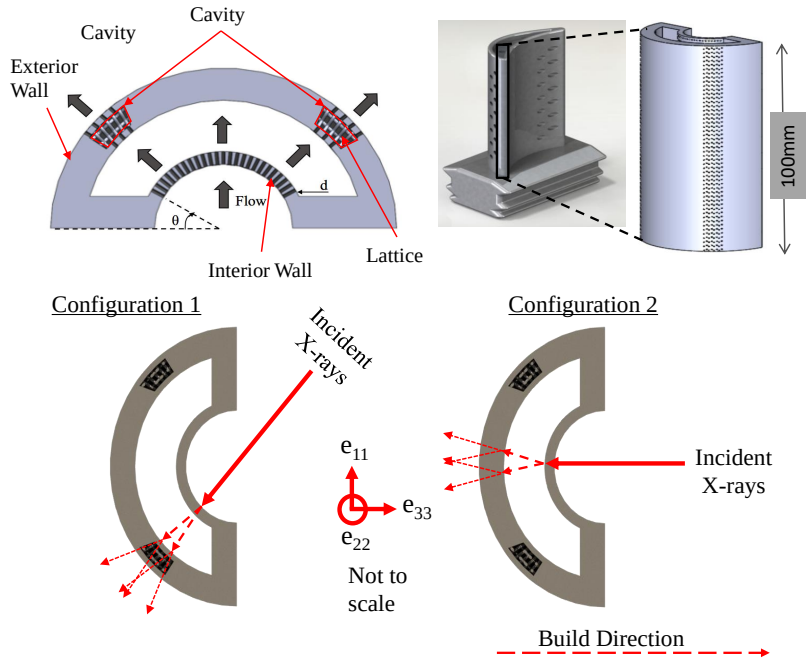

Figure 3.8: Sample orientations to obtain orthogonal strain measurements through solid AM wall and AM lattice structure.

3.5 2-D X-ray Diffraction Analysis Procedure

3.5.1 2-D XRD Analysis Procedure for TBC measurements

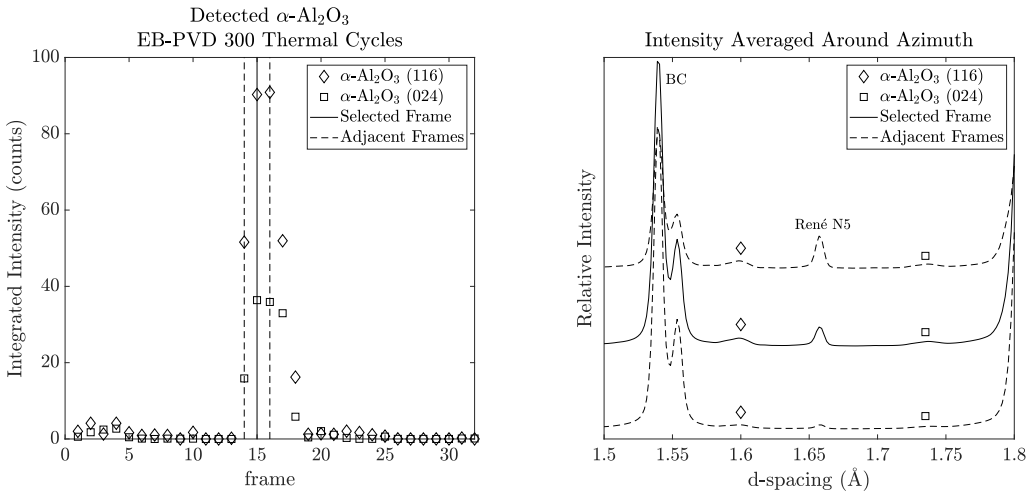

Figure 3.9: Detected integrated intensity for one file of TGO at each frame. Selected frame used for strain calculations.

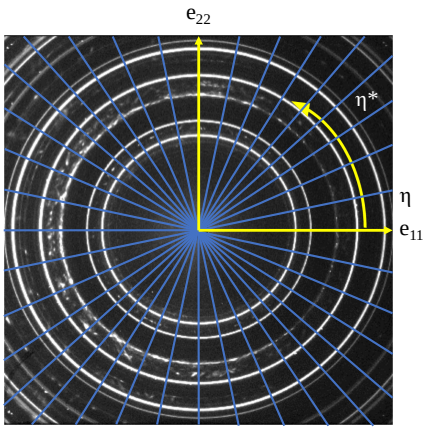

Figure 3.10: Blue lines indicate sections of rings analyzed. This process is known as caking.

The intensity vs. d-spacing plots averaged around the azimuth were analyzed for multiple phases of Al_2O_3 and YSZ, shown in Figure 3.11. In 2D XRD, lattice planes with a lower d-spacing create larger diffraction rings which are more sensitive to strain. In this experiment, (116) and (024) α–Al_2O_3 lattice planes were analyzed due to their small d-spacing, isolation from surrounding peaks, and relatively high intensity compared to other α–Al_2O_3 lattice planes.

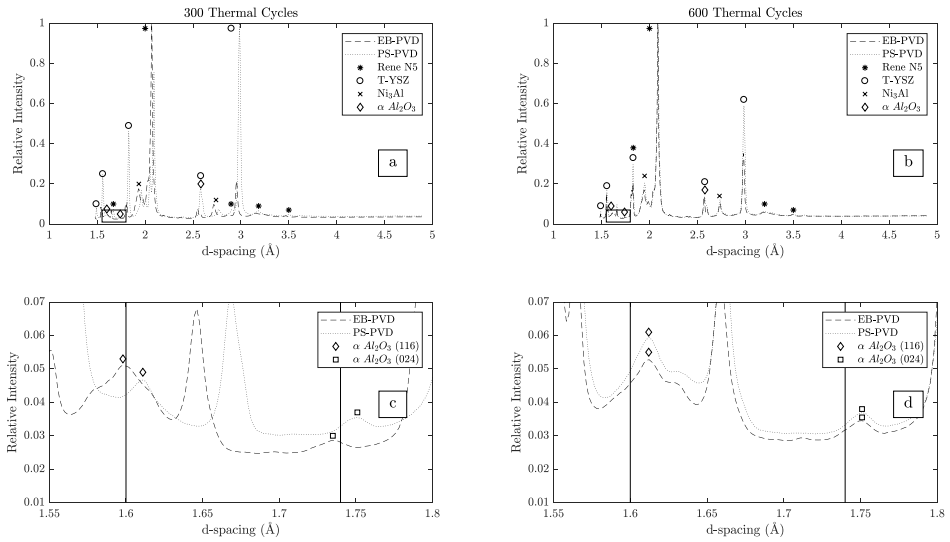

Figure 3.11: X-ray diffraction lineout plots at the location of the TGO after 300 thermal cycles (a & c), and 600 thermal cycles (b & d). The insets of these lineout graphs indicate multiple α-Al_2O_3 peaks used for the strain calculations.

For the TGO study, the frame within each file to be investigated for this was determined by plotting the integrated intensity of the α - Al_2O_3 (116) and (024) lattice planes for each frame. The frame with the highest intensity was chosen for strain calculations. The frame selection process is shown in Figure 3.9.

The diffraction pattern was collected by the 2048 x 2048 pixel grid detector resulting in intensity readings I(R,η), where R denotes the radial distance from the center of the detector to the pixel being investigated and η is the azimuthal angle between the horizontal reference and the radial distance, R [84, 76]. The diffraction rings, plotted in polar coordinates, were divided into sections at azimuthal intervals with a bin size of 10°, creating 36 total radial lineouts. These were then averaged for each radial position and converted to d-spacing by Bragg's law.

A strain-free reference angle for each diffraction ring, η*, was measured for the strain free radial position, R_0, and implemented into the strain equation, $\varepsilon = (R_0\text{-}R)/R$. This angle was calculated with the X-ray elastic constants $S_1(hkl)$ and $S_2/2(hkl)$ [76, 59]. The elastic stiffness constants C_{ij} for α-alumina [5] were used to calculate the X-ray elastic constants using DecCalc software [85]. X-ray elastic constants are material specific, as shown in Table 3.1, and were calculated by the Kröner-Eshelby method [86].

Table 3.1: Material stiffness constants used for orthogonal strain calculations for α-Al_2O_3 [5], *t*-YSZ [6], and γ–Amdry 1718 [89]

Element	Elastic Stiffness Constants (GPa)						
	C_{11}	C_{12}	C_{13}	C_{14}	C_{33}	C_{44}	C_{66}
Al_2O_3	497	163	119	-19	501	147	-
YSZ	451	240	50	-	302	39	82
Amdry 1718	248	152	-	-	-	125	-

Table 3.2: X-ray elastic constants used to calculated orthogonal strain for α-Al_2O_3, *t*-YSZ, and γ–Amdry 1718

Phase-Element	h k l	S_1	$S_2/2$
α-Al_2O_3	1 1 6	-6.16E-7	3.22E-6
α-Al_2O_3	0 2 4	-5.58E-7	3.03E-6
t-YSZ	1 0 1	-1.36E-6	5.57E-6
γ-Amdry 1718	1 1 1	-9.9E-7	4.78E-6

The (116) peak was fit in these lineouts using pseudo-Voigt functions to obtain radial values R_η for each azimuthal bin. Both the in-plane strain (ε_{22} located at η = 90°, 270°) and out-of-plane

strain (ε_{11}, located at η = 0° and 180°) were calculated with the resulting bistrain plots. It should be noted that this study only reports deviatoric strain and not hydrostatic strain, as the hydrostatic strain expands the diffraction ring uniformly around the azimuth but does not alter the angle at which the strain-free reference is calculated. The deviatoric strain values were converted to stress using Equation 3.2 [59]. Strain in the e_{22} direction, ε_{22}, was assumed to be equal to the strain in the e_{33} direction, ε_{33}.

$$\sigma_{22} = \frac{1}{\frac{1}{2}S_2}\left(\varepsilon_{22} - \frac{S_1}{\frac{1}{2}S_2 - 3S_1}(2\varepsilon_{22} + \varepsilon_{11})\right) \tag{3.2}$$

The (101) tetragonal YSZ peak (*t*-YSZ) was chosen for strain investigations due to its isolation from surrounding peaks and high intensity. The peak was fit and evaluated for in-plane (ε_{22}) and out-of-plane (ε_{11}) directional strain. The elastic stiffness constants C_{ij} for *t*-YSZ [6] are shown in Table 3.1 and were used to calculate the X-ray elastic constants using DecCalc software [85] which are shown in Table 3.2.

The monoclinic phase volume fraction (mPVF) through depth of the YSZ layer was calculated during one thermal cycle. The $(\bar{1}11)$ and (111) monoclinic peaks and the (101) tetragonal peak were fit using a pseudo-Voigt function and their respective integrated intensities were calculated. Using the integrated intensity averaged over the azimuth, η, for the investigated lattice planes, the amount of the monoclinic and tetragonal phase within the YSZ layer can be calculated. The mPVF (%) was calculated using Equation 3.3, known as the polymorph method [75], where I_m and I_t are the integrated intensity values of the monoclinic and tetragonal phases of their respective Miller indices. This is assuming that the cubic phase of ZrO_2 can be assumed to be a high temperature

polymorph of monoclinic ZrO_2. [87, 88]

$$mPVF(\%) = \frac{I_m(\bar{1}11) + I_m(111)}{I_m(\bar{1}11) + I_m(111) + I_t(101)} \tag{3.3}$$

3.5.2 2-D XRD Analysis Procedure for T-cooling measurements

The (111) γ–Amdry 1718 peak was chosen for strain calculations due to its isolation from surrounding peaks as well. Because the incident beam passed through two walls, it is entirely possible multiple peaks exist under the γ identified peak; however, since this phenomenon continued to occur throughout the scan, the convoluted peak was evaluated for strain. Additionally, the γ' peak appears to be sitting on the shoulder of the γ peak. These two peaks were deconvoluted and the γ convoluted peak was fit using a pseudo-Voigt function to evaluate the two directional strains perpendicular to the build direction of the sample, e_{11} and e_{22}. The pseudo-Voigt function is a convolution of weighted Gaussian and Lorentzian fitting functions and is used primarily to most accurately describe a peak in powder diffraction.

The elastic stiffness constants C_{ij} for γ-Amdry 1718 [89] are shown in Table 3.1 and were used to calculate the X-ray elastic constants using DecCalc software [85] which are also shown in Table 3.2.

CHAPTER 4: RESULTS AND DISCUSSION

This section consists of results from synchrotron XRD experiments conducted in the APS at the Argonne National Laboratory. Samples coated with the PS-PVD and EB-PVD techniques were investigated over their expected lifetime (0, 300, and 600 thermal cycles) through the depth of the coatings. Measurements were taken at room temperature and during one thermal cycle using the in-situ experimental setup discussed in Chapter 3. Presented here are the initial results and discussion of the residual TGO strain measurements for samples with a developed TGO. Next, the YSZ top coat results in all samples are presented and discussed with supported data from some microstructure analysis and mPVF calculations. Following this, residual strains with and without a lattice structure in the outer wall of the Amdry 1718 transpiration cooling sample were investigated.

4.1 Thermal Barrier Coating Thermally Grown Oxide Investigation

4.1.1 Residual and In-situ Strain Evolution

In Figure 4.1, TGO stress during the ramp-up of in-situ thermal cycling is shown. In-plane stress was calculated using the process mentioned in Chapter 3. The TGO in the EB-PVD uncycled and PS-PVD one hour heat treated samples was not well-developed and did not result in a diffraction ring from which strain could be calculated by the η^* method discussed in Chapter 3. Error bars are data-point specific and indicate the standard deviation from the pseudo-Voigt function discussed in Chapter 3. Temperature-dependent stresses trend toward zero at high temperature corresponding to the operating temperature. In-plane compressive stresses show variation between samples, specifically at room temperature after 600 thermal cycles. To investigate this further, the room temperature results from Figure 4.1 were averaged for PS-PVD and EB-PVD samples and are shown

in Table 4.1. Lower compressive residual stress indicates possible micro-crack initiation typically imposed by oxide growth and thermal expansion mismatch of the TBC system [90].

For both EB-PVD and PS-PVD the TGO was on average under more compressive in-plane stress after 300 thermal cycles compared to after 600 thermal cycles. The average residual in-plane stress after 600 thermal cycles for PS-PVD was 15.2% lower in magnitude than the average after 300 thermal samples. The same relationship for EB-PVD was a 10.0% reduction in in-plane stress. The difference in residual in-plane compressive stress relief between the two coatings after 600 thermal cycles can be attributed to the one PS-PVD sample that exhibits a much lower in-plane compressive stress after thermal cycling.

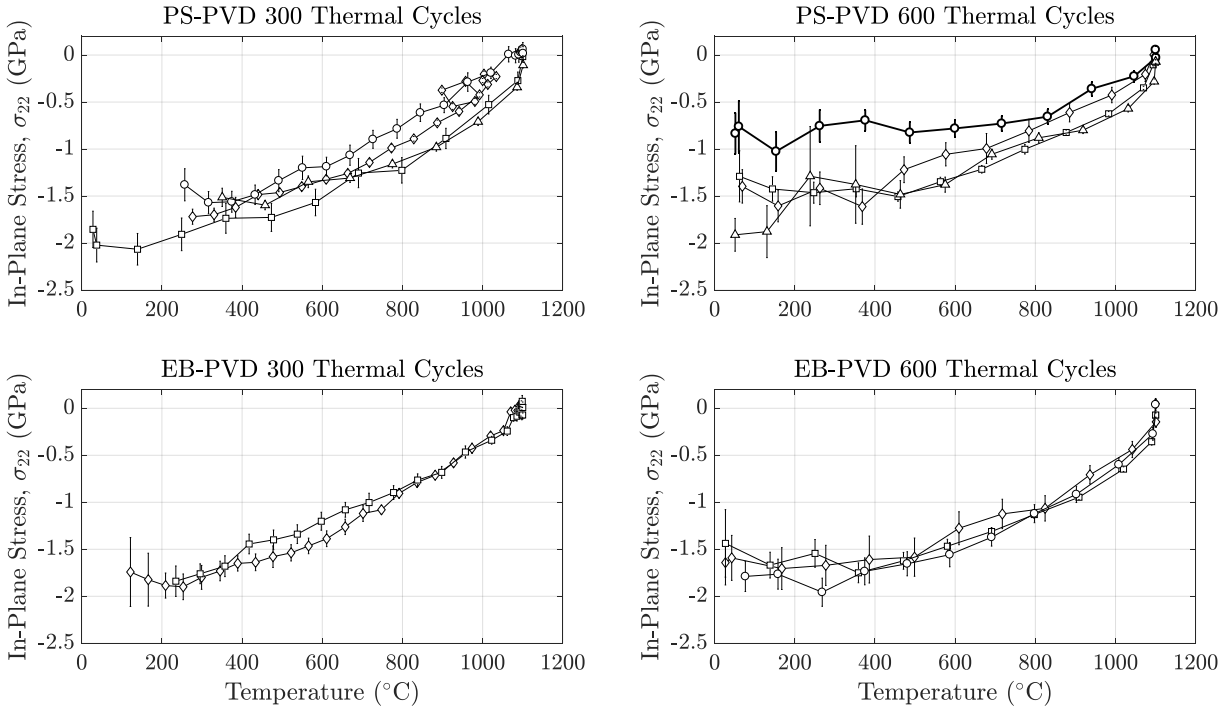

Figure 4.1: In-plane stress vs. temperature during ramp-up for all test cases. Letters denote run batch for PS-PVD samples and are arbitrary for EB-PVD samples.

Table 4.1: TGO stress measured at room temperature before XRD thermal cycle experiments.

Deposition Technique	Average in-plane (σ_{22}) residual stress (MPa)	
Number of Thermal Cycles	300	600
EB-PVD	-1760 ± 219	-1606 ± 233
PS-PVD	-1785 ± 423	-1493 ± 194

Reduced residual stress can signify an evolved TGO with increased rumpling, creating micro-cracks and potential delamination of the YSZ from the bond coat [91, 56, 92]. Presence of compressive in-plane stresses and tensile out-of-plane stresses has been reported in analytical studies [90] in the TGO of plasma sprayed systems. With orthogonal stress analysis, both compressive in-plane stresses (at the bottom of an undulation) and tensile out-of-plane stresses (at the top of the undulation) would contribute to the reduced average stress. Tensile stress in the out-of-plane (e_{11}) direction and compressive stresses in the in-plane (e_{22}) direction found in the TGO during one thermal cycle for samples of both coating methods are shown in Figure 4.2. The two directions showed a similar magnitude of stress, indicating they both can equally represent the stress relief in the TGO during thermal cycling. However, in-plane stresses are directly caused by CTE mismatch of layers and and oxide scale growth which in turn create the out-of-plane stresses that provide the driving force for oxide spallation [93].

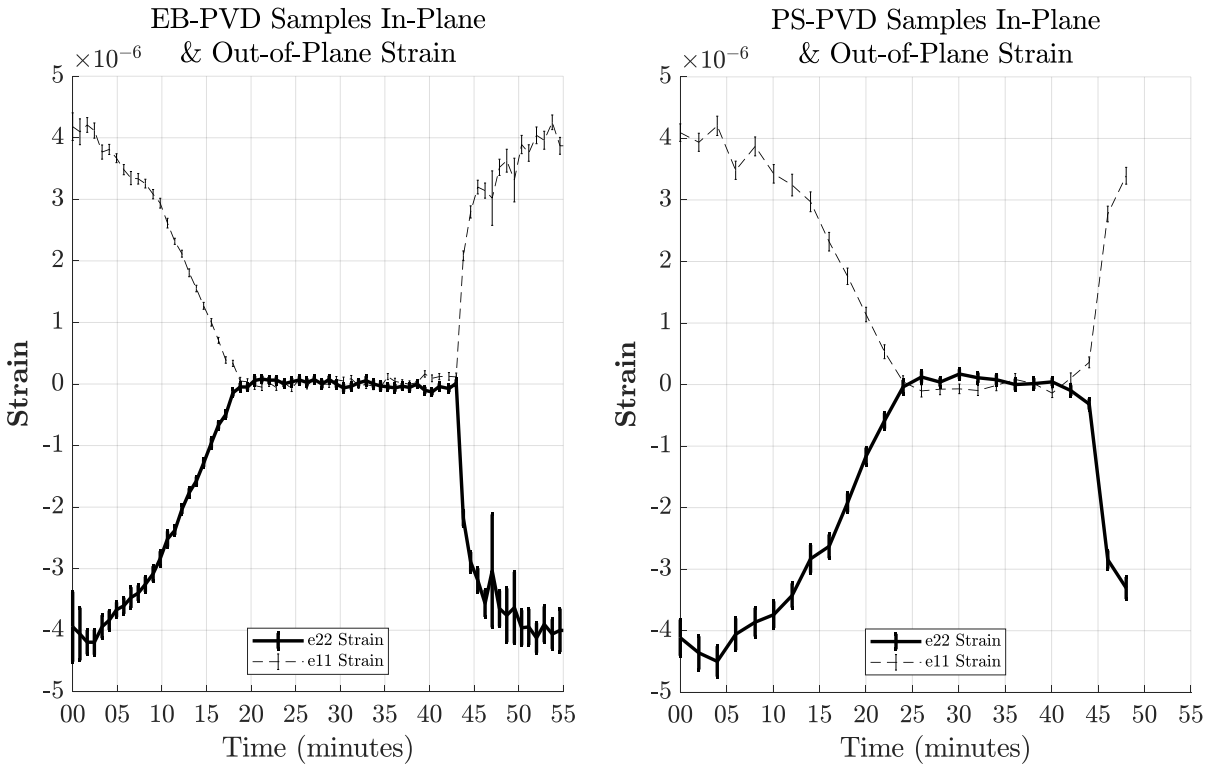

Figure 4.2: Example of in-plane and out-of-plane strain comparison of TGO grown in a 300 hr thermally cycled EB-PVD and PS-PVD samples.

Full cycle in-plane stresses are shown in Figure 4.4 and indicate both coating methods exhibit similar in-plane compressive stresses at high temperature. This similar stress at operating temperatures is attributed to the similar temperatures experienced by both coating types during the TGO formation. Samples of both coating types fluctuate around near zero stress in both e_{11} and e_{22} directions during hold times. A lattice plane comparison is presented in this figure for one sample for each PS-PVD and EB-PVD sample set after 300 thermal cycles to demonstrate the reliability of the approach for resolving deviatoric orthogonal strain. During experimentation, thermal cycle hold times were not precisely consistent across all samples and this is evident in the results shown

in Figure 4.4. The TGO in all samples achieved a relaxed state at high temperature hold as is expected. The thermal load on both the substrate and the YSZ top coat result in a thermal expansion that relieves in-plane compressive stress applied to the TGO and YSZ/bond coat interfaces during cool down. Therefore, high temperature relaxation in all samples at hold should be considered evidence of no spallation but not necessarily the absence of localized damage.

Parallel photoluminescent spectroscopy studies found the same overall increase of residual TGO stresses for both PS-PVD and EB-PVD samples after 300 thermal cycles and a similar reduction of residual stress in PS-PVD samples after 600 thermal cycles [1] as shown in Figure 4.3. Other reports also agree with this trend of increased TGO residual stresses after cycling followed by a gradual decrease in residual stresses [54]. Some reports have shown an immediate reduction in residual stresses at the TGO layer after thermal cycling which were attributed to increasing TGO thickness/roughness or crack nucleation and propagation [13]. The TGO in coatings investigated in this work differ in a number of ways but may become more similar through control of processing parameters for the PS-PVD coating technique that better replicates the EB-PVD microstructure.

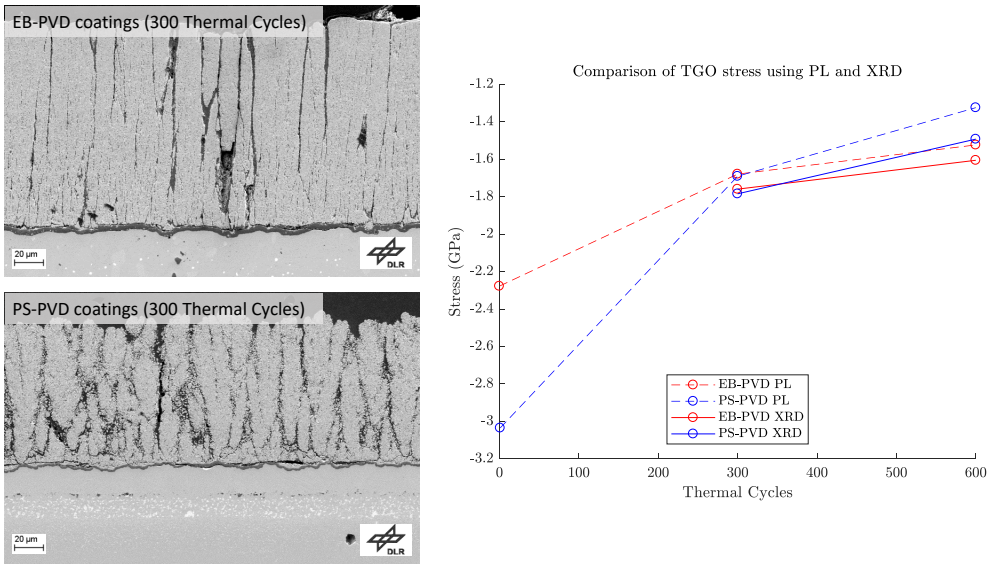

Figure 4.3: In-plane residual stresses measured with synchrotron XRD and residual stresses measured with PL on both PS-PVD and EB-PVD coatings. SEM images of both coatings shown to the left.

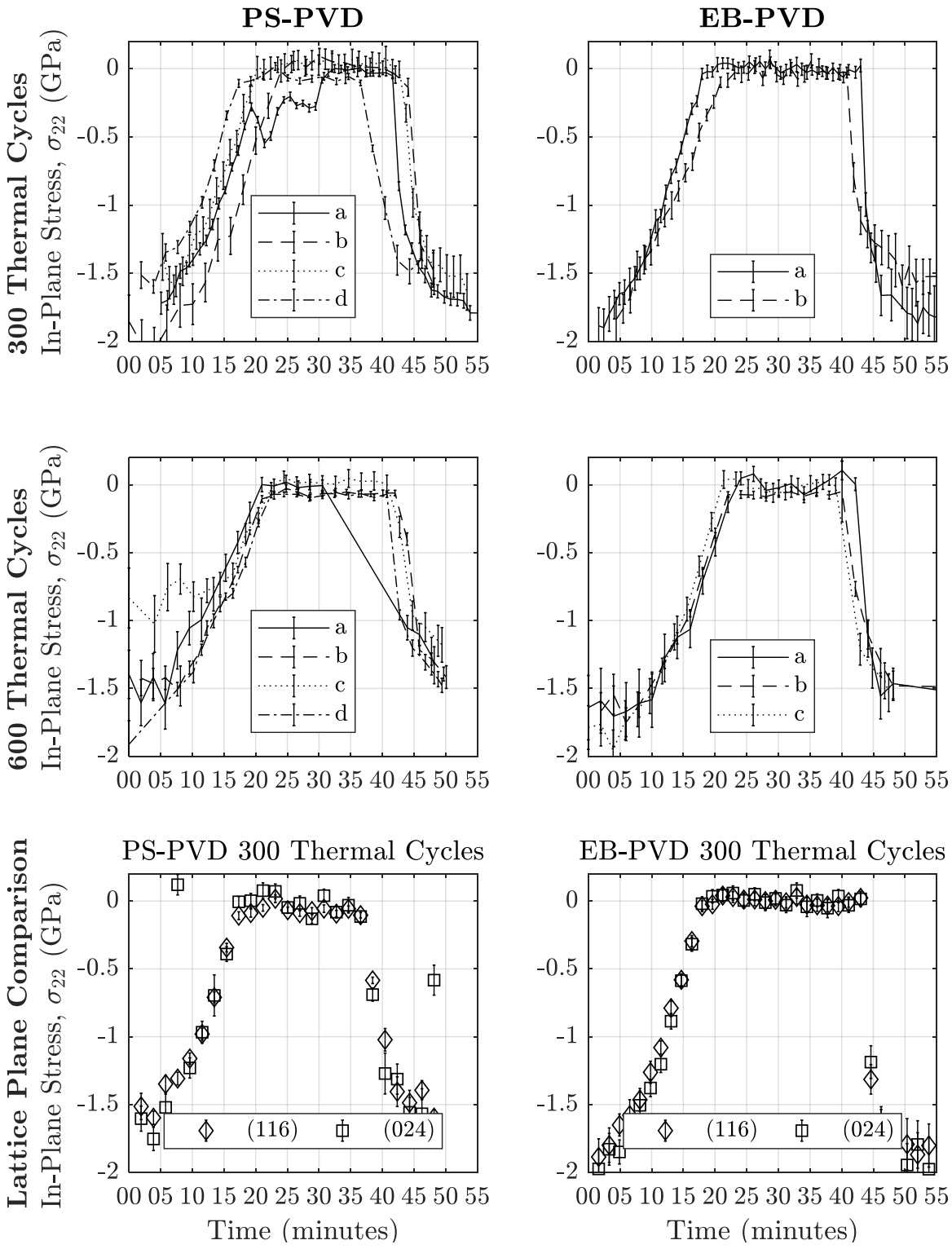

Figure 4.4: In-plane stress vs. time for one thermal cycle for all test cases.

4.1.2 SEM imaging of TGO in Thermally Cycled Samples

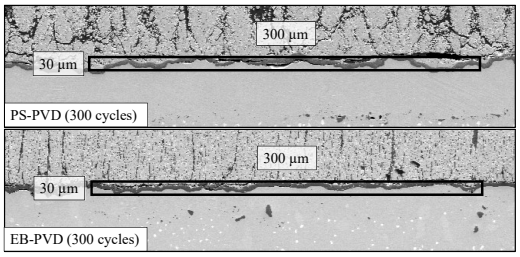

Figure 4.5: Beam window size overlaid on micrographs of TGO.

Previous SEM microstructure studies were conducted on these samples. [1] Using image processing software ImageJ with SEM images, TGO thickness was measured for both deposition methods. Both samples' TGO layers thickened and became more convoluted with thermal cycling due to the cyclic plastic deformation of the bond coat [55]. Both deposition techniques exhibited a similar average TGO thickness of 3.4 μm $\pm$ 0.8 μm after 300 thermal cycles. Both deposition methods had a similar TGO thickness after 600 thermal cycles as well, 4.1 μm $\pm$ 0.6 μm for PS-PVD samples and 3.8 μm $\pm$ 0.5 μm for EB-PVD samples demonstrating a consistent evolution of TGO thickness in both coating methods. TGO convolution in a PS-PVD sample was observed to be greater than that of an EB-PVD sample from the SEM images after 300 hrs of thermal cycling as shown in Figure 4.6a & b. After 600 thermal cycles PS-PVD samples showed a larger TGO roughness than EB-PVD samples as shown in Figure 4.6c & d. This larger TGO thickness and rumpling indicates failure modes may vary for the two deposition methods [94]. EB-PVD samples displayed localized delamination along the interface due to shear force of the TGO and YSZ while these delaminations in PS-PVD samples formed from crest to crest of the TGO layer and within the YSZ above the TGO. The greater TGO convolution in PS-PVD samples will create points of high stress concentration near the crests and troughs of the TGO which cause this intralayer delamination due to tensile stresses [95]. The delamination along the interface of the TGO and YSZ

in the EB-PVD samples may also indicate a lower bond strength at the interface of these layers than PS-PVD samples. This micro-cracking can be seen in both EB-PVD and PS-PVD samples that were thermally cycled for 300 hrs in Figure 4.6.

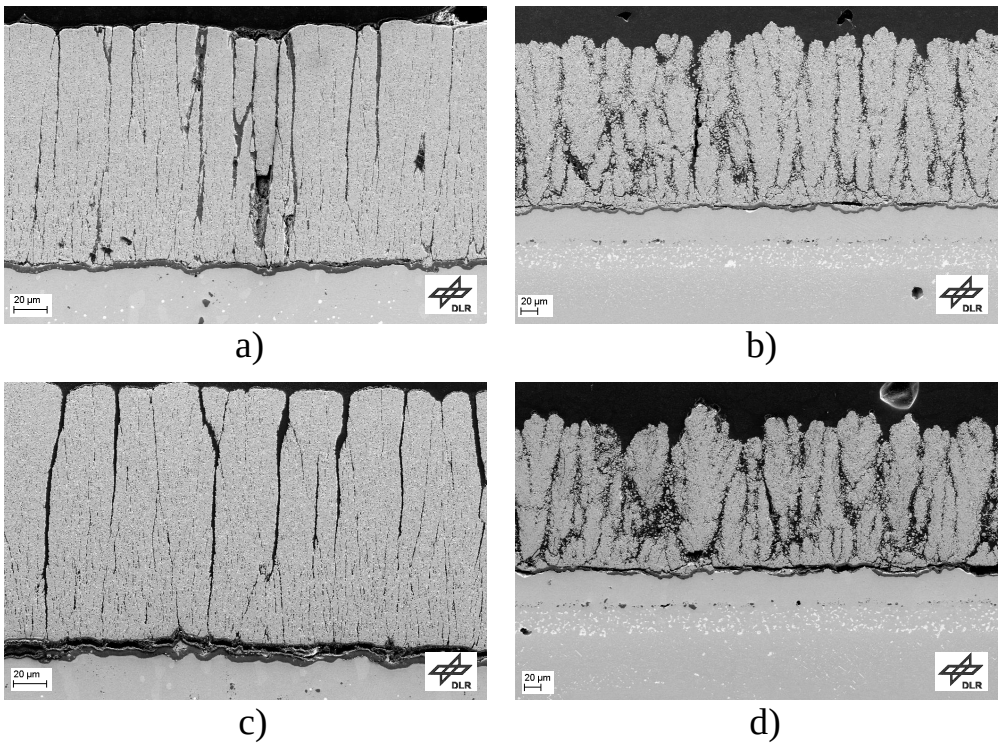

Figure 4.6: SEM images of TGO after 300 thermal cycles in a) EB-PVD and b) PS-PVD samples and 600 thermal cycles in c) EB-PVD samples and d) PS-PVD samples [1].

Additionally, the TGO layer was observed to be more porous in PS-PVD samples compared to EB-PVD samples causing intralayer cracking within the TGO. This intralayer cracking in PS-PVD samples can be attributed to a more porous TGO layer than in EB-PVD samples.

4.2 Thermal Barrier Coating YSZ Investigation

4.2.1 Residual and In-situ Strain/Stress Evolution

Samples of all thermal ages (0,300, 600 thermal cycles) were studied in the YSZ investigation. Figure 4.7 shows the interface compressive in-plane residual strains in both coating methods at the YSZ/TGO interface over their respective lifetimes. Figure 4.8 shows the tensile out-of-plane residual strains at the YSZ/TGO interface for the same samples. The shaded region is the representative trend of strain found in each coating method's stage of lifetime. This comparison shows consistently higher magnitudes of in-plane compressive strain compared to the out-of-plane tensile strains throughout all stages of lifetime. This indicates the in-plane compressive strain will have a greater effect on micro-cracking and delamination than the out-of-plane directional strain.

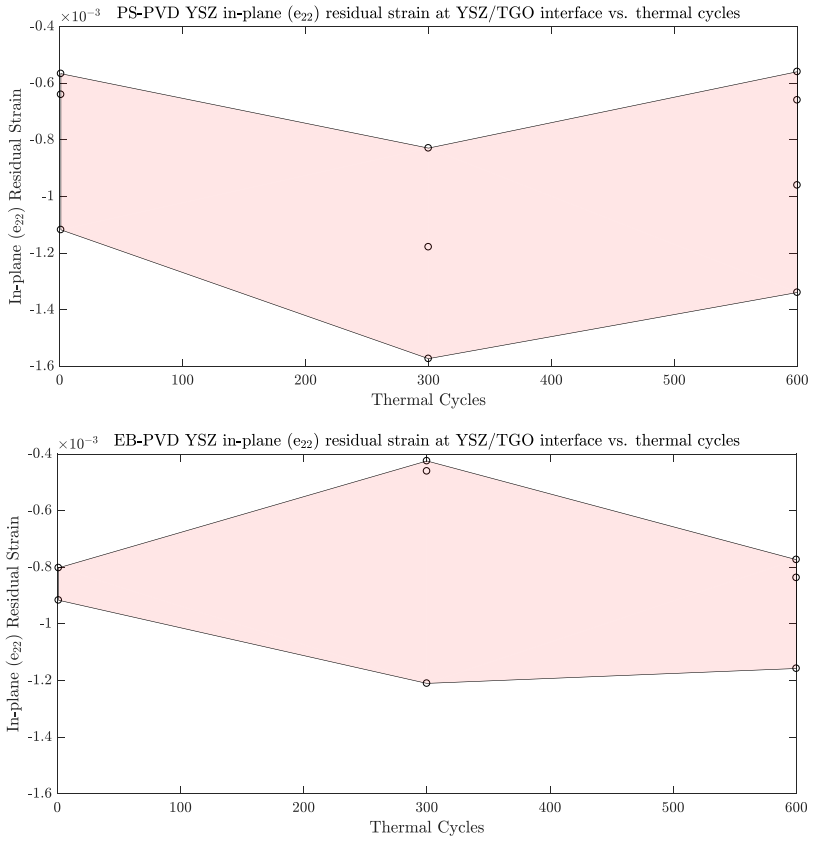

Figure 4.7: YSZ/TGO in-plane interface strains in samples throughout lifetime in both PS-PVD and EB-PVD samples.

Reduced strains found in the YSZ indicate possible micro-cracking within the top coat. PS-PVD samples, in general, exhibited higher residual in-plane strain at the YSZ/TGO interface after 300 thermal cycles compared to uncycled samples. This in-plane compressive strain was then relieved after 600 thermal cycles. This indicates micro-cracks have possibly formed within the YSZ coating. EB-PVD samples showed, in most cases, a decrease in residual in-plane compressive strain at the interface after 300 thermal cycles correlated with YSZ top coats that have been separated from their bond coats [96] indicating these EB-PVD samples are experiencing much lower YSZ/bond

coat adhesion. After 600 thermal cycles, and unexpected increase in compressive in-plane strain was exhibited in EB-PVD samples. PS-PVD samples exhibited, in general, greater in-plane compressive stress at the YSZ/TGO interface than EB-PVD samples. This insinuates greater bond coat adhesion in PS-PVD samples which correlates to the greater TGO convolution as shown in Section 4.

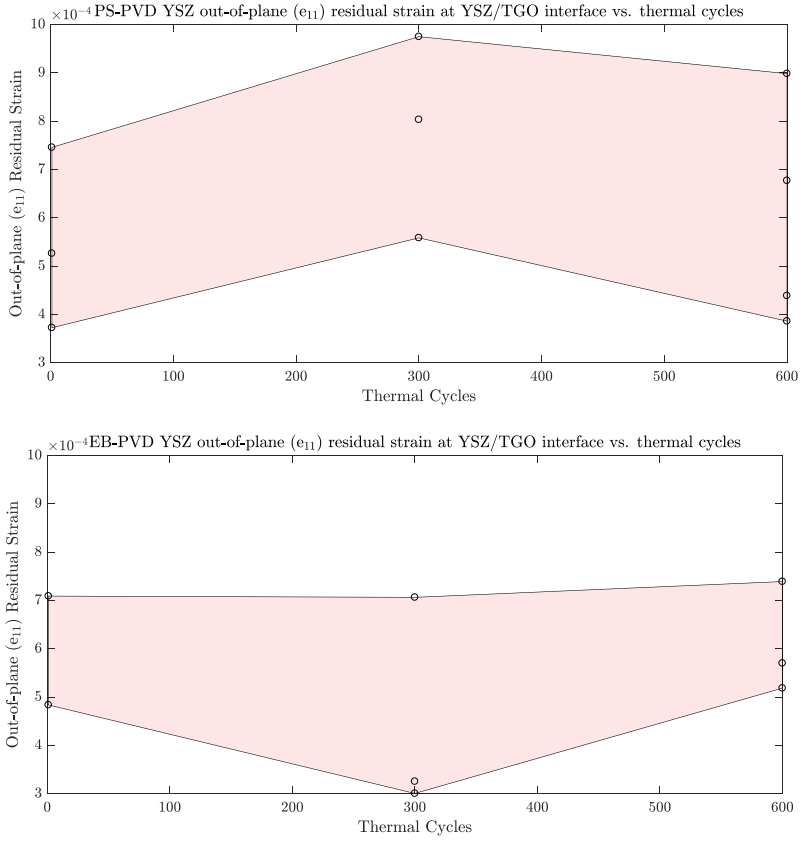

Figure 4.8: YSZ/TGO out-of-plane interface strains in samples throughout lifetime in both PS-PVD and EB-PVD samples.

In-plane YSZ strains were converted to stress using the biaxial thin film assumption mentioned in Chapter 3. Residual and in-situ in-plane stresses through the top coat are shown in Figure 4.9 for

PS-PVD samples at different points of lifetime. Different colors indicate different temperatures the top coat experienced within a thermal cycle. Error bars are data-point specific and indicate the standard deviation from the pseudo-Voigt function discussed in Chapter 3. PS-PVD samples after one hour of thermal cycling are designated as uncycled samples for simplicity. Uncycled PS-PVD samples exhibited in-plane tensile stresses, typical of APS coatings. In-plane compressive stresses experienced at the top surface of PS-PVD coatings are zero throughout the thermal cycle. This is also similar to APS coatings. This indicates a possible greater localization of stress in PS-PVD samples at the YSZ/TGO interface compared to EB-PVD samples. This greater interface stress is indicates greater adhesion between the YSZ and TGO layers. As temperatures increase, the YSZ/TGO interface in-plane compressive stress trends towards zero. This is due to the zero-stress state of the TGO as discussed in Section 4 [37, 56].

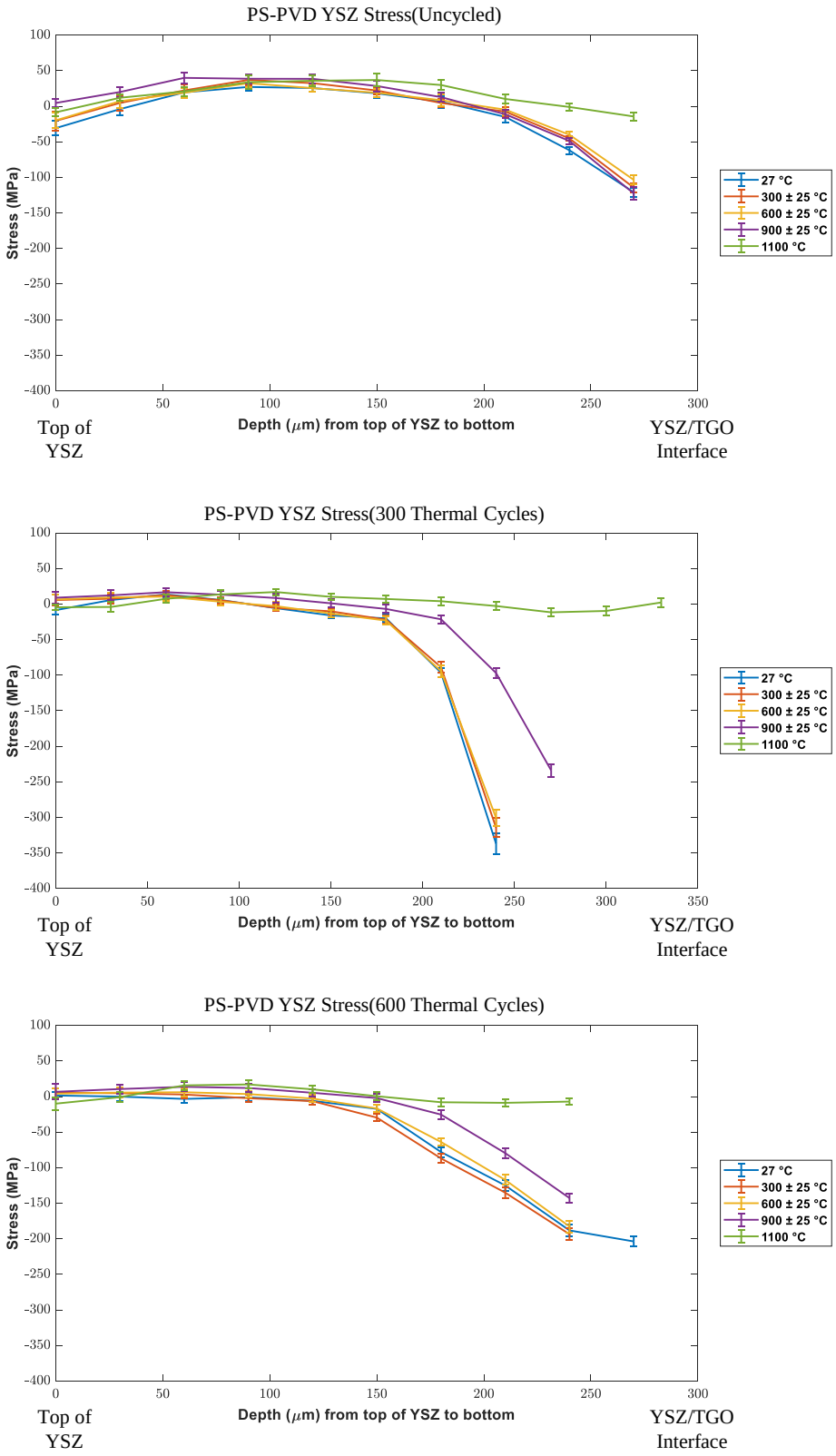

Figure 4.9: Through depth in-plane YSZ stress over one thermal cycle for one representative PS-PVD sample at various stages of lifetime.

EB-PVD samples were measured as well over one thermal cycle throughout the YSZ top coat. In-plane compressive stresses for these samples are displayed in Figure 4.10. Temperatures for each through depth measurement deviated by approximately 25°C due to the scans being run across each TBC system while temperatures were ramped up. EB-PVD samples exhibited greater compressive in-plane stress at the top of the YSZ than PS-PVD samples. EB-PVD samples after 300 thermal cycles also generally showed this in-plane compressive stress at the top of the YSZ with a slightly increased in-plane compressive stress at the YSZ/TGO interface. This indicates a lower adhesion between the YSZ and bond coat layer in EB-PVD samples [96]. The trend of increased in-plane compressive stress closer to the YSZ/TGO interface is exhibited in samples of both coating methods. At high temperature, in-plane compressive stress for both coating types relax to zero throughout the top coat. This is expected as the TGO growth and CTE mismatch induced stresses are less influential at high temperature.

Table 4.2: Previous YSZ stress and strain results of various testing methods on EB-PVD, PS-PVD, and APS thermal barrier coatings. The top row shows the findings from this study.

Authors	Coating method	Measurement Location	Measurement Technique	Max Residual stress YSZ (Uncycled to Lifetime)	Max Residual strain YSZ (Uncycled to Lifetime)	Maximum Cycling
Northam, Raghavan	EB-PVD/PS-PVD	Through depth	XRD	-100 MPa to -200 MPa/ -150 MPa to -350 MPa	-9x10^{-4} to -1.2x10^{-3}/ -9x10^{-4} to -1.6x10^{-3}	600 Thermal Cycles
Tanaka [97]	EB-PVD	Through depth	Raman	-220 MPa	-	As-deposited
Yang, Tao [54]	PS-PVD	Top surface	Raman	0 to -75 MPa	-	200 Thermal Cycles
Yang, Tao [13]	PS-PVD	Top surface	Raman	100 to -175 MPa	-	300 Thermal Cycles
Weyant [37]	APS	Through depth	XRD	-150 MPa	-	112 hour heat treatment
Rossmann, Raghavan [1]	EB-PVD/PS-PVD	Through depth	Raman	-220 to -400MPa/ -50 to -400MPa	-	600 Thermal Cycles
Thornton [58]	APS	Through depth	XRD	-	-5x10^{-4}	21 hour heat treatment
Tomimatsu [48]	EB-PVD	Top surface	Raman	200 to -300 MPa	-	As-deposited
Knipe, Raghavan [79]	EB-PVD	Through depth	XRD	-	-2x10^{-3}	As-deposited

Studies using Raman spectroscopy on free standing EB-PVD coatings exhibited similar increasing compressive stress trends through depth closer to the YSZ/TGO interface [96]. In another

study, stresses found through depth of PS-PVD coatings showed tensile stresses near the top of the YSZ layer which then decrease to compression near the YSZ/TGO interface in the as-deposited state [13]. In cycling studies, after 50 thermal cycles, these tensile stresses also changed to compression [54]. Differences between stresses and strains found in other studies using varying testing techniques and this study using synchrotron X-ray diffraction is shown in Table 4.2.

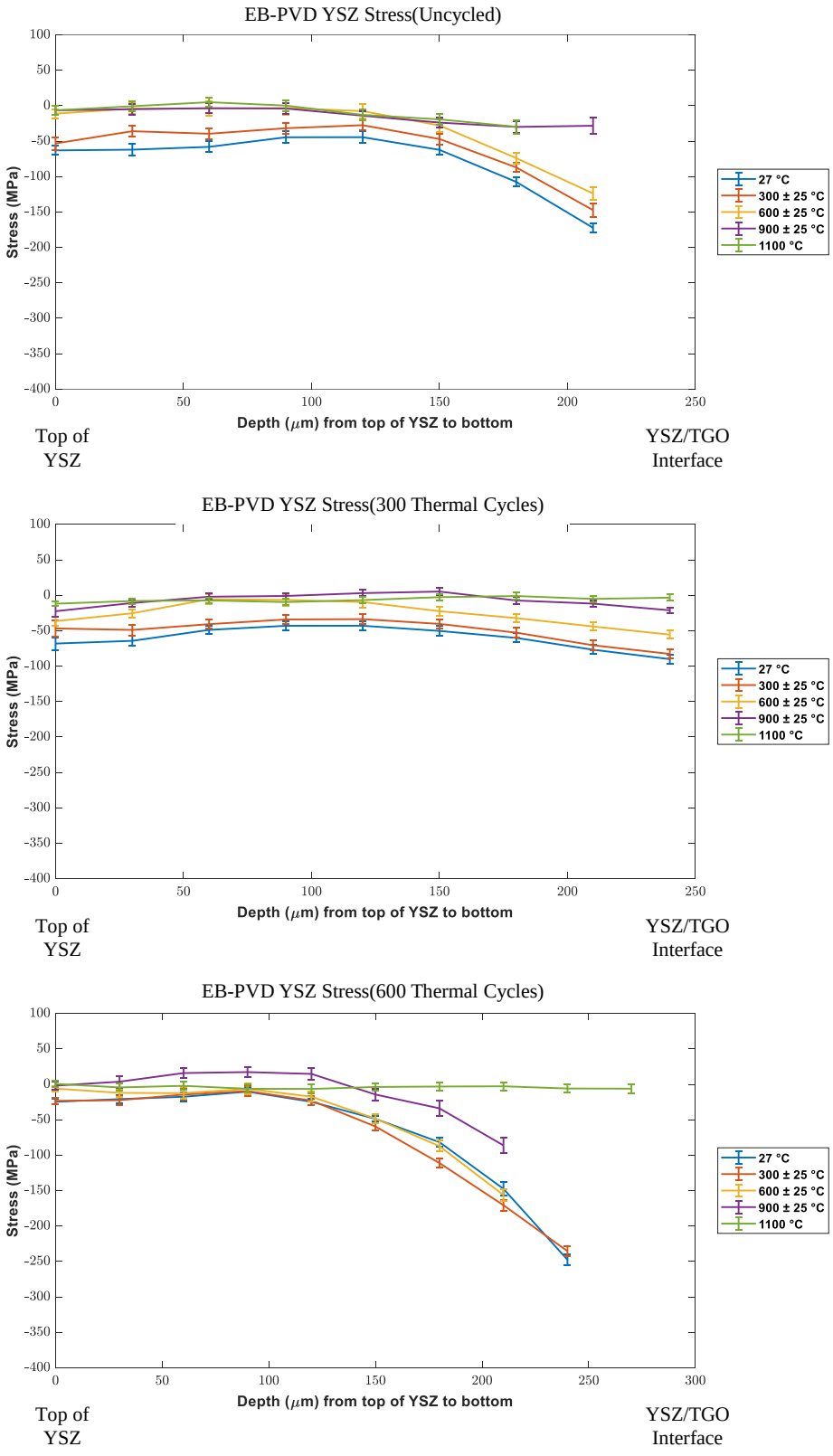

Figure 4.10: Through depth in-plane YSZ stress over one thermal cycle for one representative EB-PVD sample at various stages of lifetime.

4.2.2 In-situ YSZ Phase Volume Fraction

The mPVF (%) in samples of both coating methods were examined through depth of the YSZ over their lifetime (0,300,600 thermal cycles). Results displayed in Figure 4.11 show the mPVF found in EB-PVD samples correlated to the coatings' in-plane stresses measured during one thermal cycle. mPVF is represented by color with the respective values shown in the color bar to the right of each plot. Changes from tetragonal to monoclinic phase has a known volumetric expansion of about 4% which create compressive stresses in surrounding materials and vice versa [22]. EB-PVD samples exhibited a consistently higher mPVF at the both the top and bottom surfaces of the YSZ top coat. mPVF in EB-PVD samples then lowered to zero at high temperature due to the martensitic phase change from monoclinic to tetragonal at approximately 600 °C. This decrease in mPVF creates a reduction in volume of the unit cells wihtin the YSZ, increasing tensile stresses in this region [27]. This indicates the mPVF plays a factor in the reduction of in-plane compressive stresses found in EB-PVD YSZ top coats.

Uncycled EB-PVD samples exhibited close to zero mPVF. This is due to the formation of the "non-transformable" tetragonal phase, t', during deposition which is consistent with literature regarding EB-PVD [22, 98]. This is the most desired phase in industry due to its unique tweed microstructure, including lattice distortions such as antiphase boundaries, that creates a better thermomechanical response [99]. After 300 thermal cycles, EB-PVD samples show greater mPVF at the top and bottom of the YSZ top coat. This is possibly due to the sintering of columns due to thermal cycling which cause phase transformations from the stable t' phase to a combination of tetragonal and cubic phases followed by monoclinic and cubic phases [25].

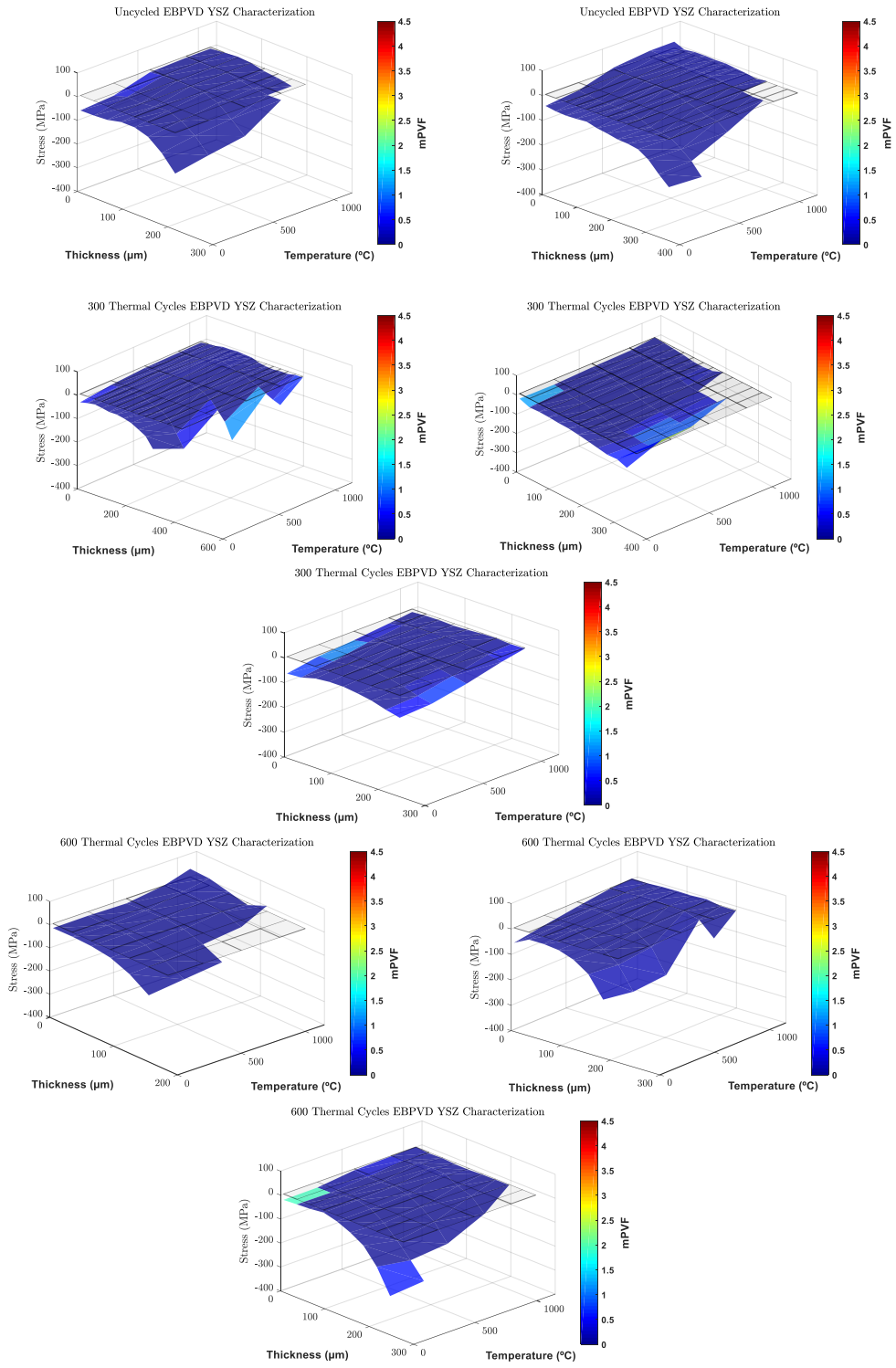

Figure 4.11: YSZ stresses through depth during single thermal cycle for 1) Uncycled (2 samples) 2) 300 cycles (3 samples) 3) 600 cycles (3 samples) EB-PVD coated samples. Stresses displayed in the Z-direction. Colors represent mPVF at each data point.

PS-PVD samples showed a much greater presence of the monoclinic phase throughout the YSZ as shown in Figure 4.12. This indicates that during the cooling of deposition, the YSZ does not result in the same t' phase that exists in as deposited EB-PVD coatings. This is most likely due to the differences in deposition temperatures of the two coating methods [2, 100]. Alternatively, as PS-PVD microstructure is less homogeneous, it is possible that the powders injected into the feedstock were not fully vaporized, creating concentrations of monoclinic ZrO_2. Although it has been shown in studies that slow increases in temperature such as the one PS-PVD samples experienced during heat treatment have led to increased formation of the monoclinic phase in the YSZ top coats of TBCs [24]. In these highly concentrated areas, the monoclinic phase will then decrease after 600 °C and, presumably, alter the stresses through the depth of the YSZ.

Particularly, the monoclinic phase in PS-PVD appears to congregate in the center of the YSZ; however, this phase still exists in a larger quantity at the YSZ/TGO interface at room temperature compared to EB-PVD as shown in Figure 4.12. As temperature increases the mPVF across the top coat decreases toward zero due to the martensitic phase change experienced also in EB-PVD samples [98]. Normally the CTE mismatch between layers causes an expansion and contraction at the TGO/YSZ interface [101]. Because of this phase change with temperature however, over hundreds of cycles this expansion and contraction could be amplified, accelerating the rumpling of the TGO layer. This difference in TGO convolution can also be seen through SEM imaging after 300 hours of thermal cycling for both deposition methods in Figure 4.6.

Studies using X-ray diffraction to study the phases found in PS-PVD samples indicated no monoclinic phase after deposition [2]. This indicates the monoclinic phase found in the samples of this study to be the results of the slow rate of temperature increase during heat treatments. While mechanical and material properties such as in-plane stress and mPVF through depth of the two coatings differ changes in the processing parameters of PS-PVD coatings may reveal similarly performing TBCs over lifetime.

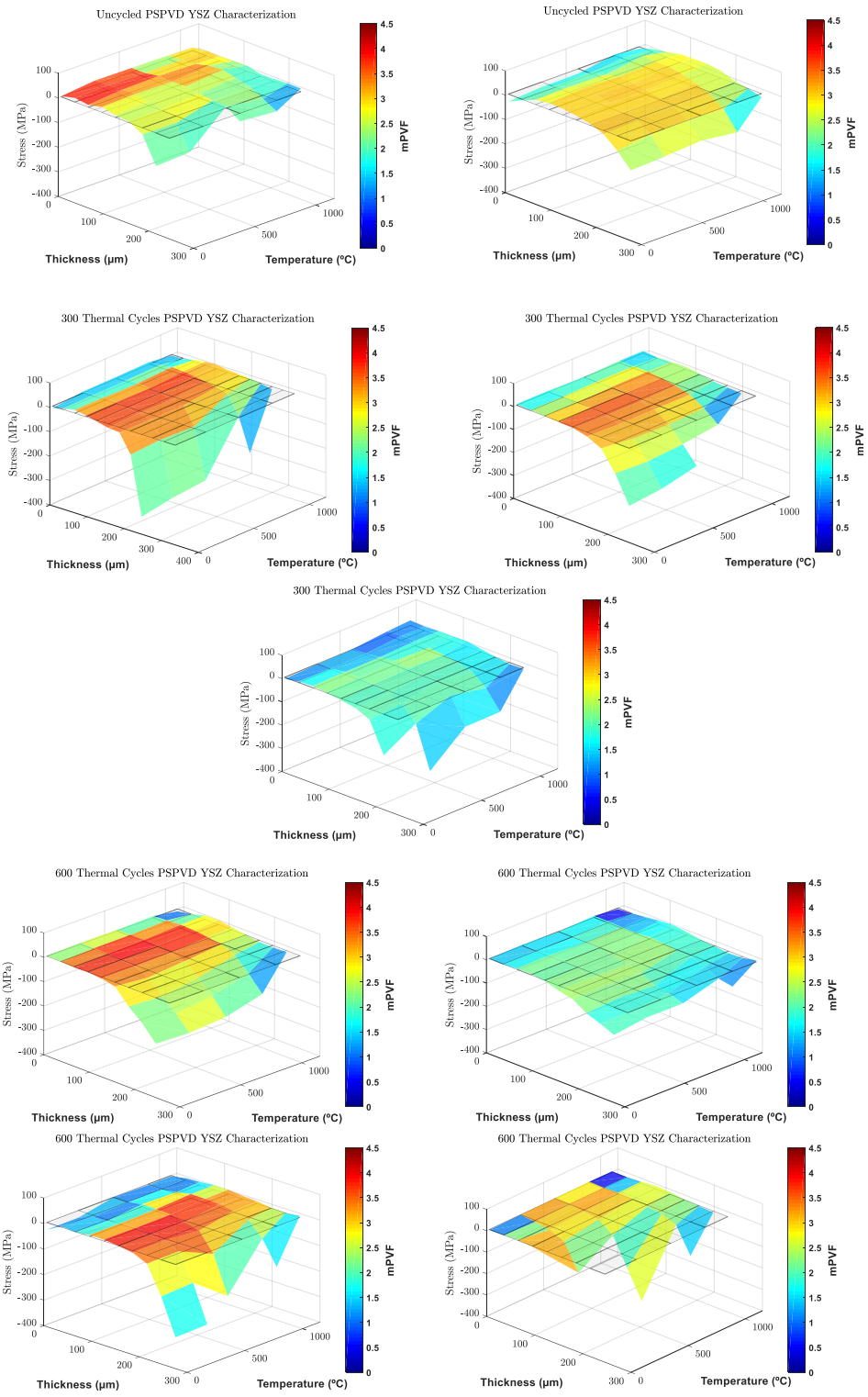

Figure 4.12: YSZ stresses through depth during single thermal cycle for 1) Uncycled (2 samples) 2) 300 cycles (3 samples) 3) 600 cycles (4 samples) PS-PVD coated samples. Stresses displayed in the Z-direction. Colors represent mPVF at each data point.

4.2.3 SEM imaging of TGO in Thermally Cycled Samples

SEM images were taken on TBC systems with both coating methods through different stages of their lifetime. Figure 4.13 shows YSZ top coats of EB-PVD samples in the first row and PS-PVD samples in the second row. Both coating methods show a similar columnar microstructure that was intended for this comparison study. PS-PVD samples showed a greater top coat surface roughness than that of EB-PVD samples. Higher surface roughness can cause flow separation of air film cooling, increasing the temperatures experienced in the TBCs and aerodynamic efficiency loss through the early stage turbine blades [26]. PS-PVD samples also exhibited greater intercolumnar gaps compared EB-PVD coated samples. Intercolumnar gaps in samples of both coating methods increased with thermal cycling. This can be attributed to sintering of columns after thermal cycling. This sintering increases thermal conductivity and YSZ Young's modulus, lowering the lifetime of the coating [21, 102].

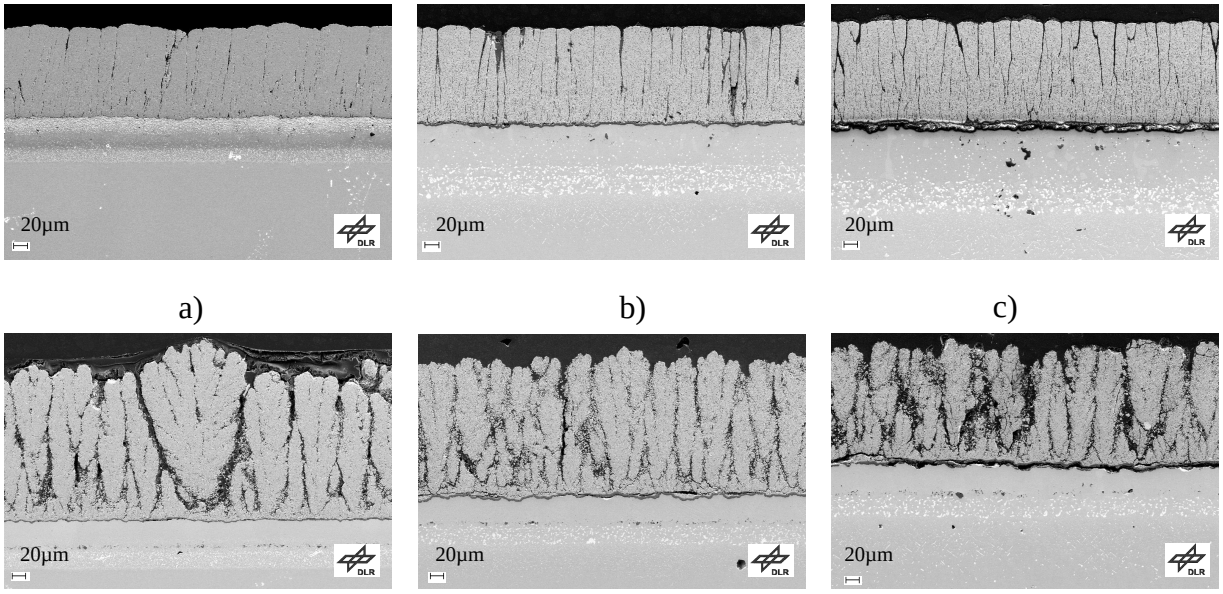

Figure 4.13: SEM images of YSZ top coat in EB-PVD samples after a) 0 thermal cycles b) 300 thermal cycles and c) 600 thermal cycles and PS-PVD samples after d) 1 hour heat treatment e) 300 thermal cycles and f) 600 thermal cycles [1].

4.3 Additively Manufactured Amdry 1718 Investigation

4.3.1 Residual and In-situ Strain/Stress Evolution

Intensities averaged around the azimuth of the X-rays diffracting from the γ-Amdry 1718 (111) lattice plane in both the AM lattice structure and solid wall are shown in Figures 4.14a and 4.14d respectively. Peaks in mean intensity shown are due to the X-ray passing through the AM holes on the interior wall of the sample. Mean intensities in the map of the lattice structure shows

greater intensities in the region of the cavity containing the lattice structure. This intensity lowers to values similar to the intensities found in the AM solid wall map, indicating the point at which measurements were no longer being taken in the lattice structure cavity. Higher intensities will be found in measurements of the lattice structure because of less material in the cavity compared to the solid wall.

Residual strains and overall intensity readings found within the AM lattice structure are shown in Figures 4.14b and 4.14c. All measured strains were perpendicular to the build direction. Strains found within AM solid wall are shown in Figures 4.14e and 4.14f. Strains found in both e_{11} and $_{22}$ directions vary much more so in the lattice structure compared to the AM solid wall. This is most likely due to the increased amount of deformities that occur in AM complex geometries. Variations in strain found in Figures 4.14b and 4.14c correlating with variations in intensity further indicate the complex geometry of the lattice structure plays a role in the residual strains found within the AM sample.

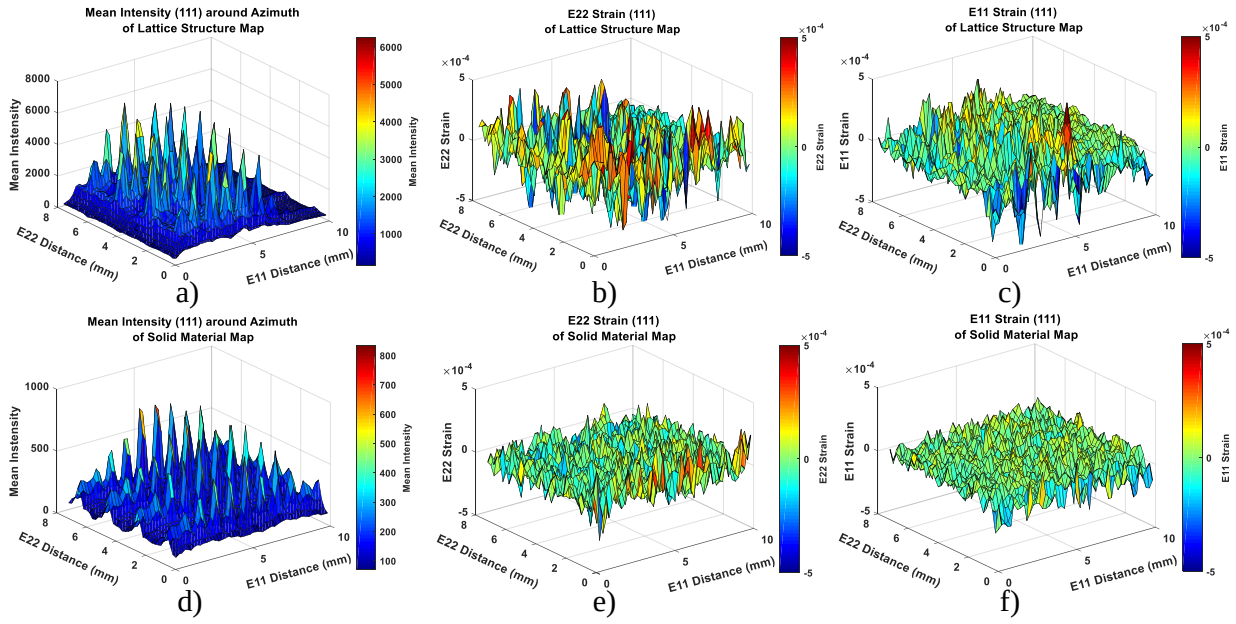

Figure 4.14: Mapping within lattice structure of AM γ–Amdry 1718 sample's a) Mean azimuthal intensity b) e_{22} strain and c) e_{11} strain. Below are mappings within solid material of AM γ–Amdry 1718 sample's d) Mean azimuthal intensity e) e_{22} strain and f) e_{11} strain.

It should be noted that these findings are preliminary and further investigations looking at the strains found in the AM lattice structure compared to solid AM material is needed to better understand how the effect of strain will be reduced when a thermal load is applied to the sample.

CHAPTER 5: CONCLUSION

These conclusions here summarize the effects of thermal management in turbine blades with respect thermal barrier coatings and additively manufactured transpiration cooling holes.

5.1 TBC Findings

In this work, the similarities and differences of PS-PVD and EB-PVD coatings are investigated through thermal cycling. Specifically the strain responses through depth of the YSZ and TGO are measured and converted to deviatoric stress through one thermal cycle using high energy synchrotron X-ray diffraction.

5.1.1 TGO Findings

The results show a similar in-plane residual stress after 300 and 600 thermal cycles for both deposition methods except for one PS-PVD sample, demonstrating that microcracks at the TGO layer will form at the same rate for both PS-PVD and EB-PVD samples. However, the PS-PVD samples had greater variance, which was not seen in EB-PVD samples, likely due to the understanding and development in the EB-PVD coating process. The measured room temperature compressive strain in the in-plane direction of the TGO was relieved after 600 thermal cycles for both deposition methods. This indicates potential corresponding microdamage, caused by stress concentrations arising from the increased thickness and convolution of the TGO with thermal cycling. This is consistent with the micrographs, which show the 600-cycle samples have a thicker and more convoluted TGO than the 300-cycle samples for both coating types. PS-PVD samples exhibited cracking from crest to crest of the TGO undulations while the EB-PVD samples cracked predominantly along the

interface of the TGO and YSZ. These differences in failure modes are due to the contrasting TGO roughnesses in each deposition method which potentially stem from the difference in YSZ porosity at the YSZ and TGO interface. All samples exhibited the same stress relaxation during hold at high temperatures, indicating continuous contact and absence of spallation between the TGO and YSZ/bond coat during thermal cycling.

5.1.2 YSZ Findings

In-plane and out-of-plane YSZ top coat strains were measured through depth of the two coating methods over lifetime in one thermal cycle. In-plane strains were then converted to stress. This included in-plane residual stress at the YSZ/TGO interface. PS-PVD samples exhibited consistently higher in-plane stresses over lifetime at this interface, indicating better adhesion between the YSZ and TGO layers. In-plane residual compressive stresses were relieved at the YSZ/TGO interface in PS-PVD samples after 600 thermal cycles, demonstrating microcrack formation within the YSZ top coat for these samples. This differs from the EB-PVD samples which showed an increasing trend of YSZ/TGO interface in-plane compressive stresses. EB-PVD coatings showed greater compressive stresses at the top of the YSZ layers compared to PS-PVD samples, demonstrating a better distribution of strain energy throughout the top coat compared to PS-PVD coatings. In the as deposited state, PS-PVD samples exhibited tensile in-plane stresses, typical of APS coatings. PS-PVD samples also showed greater mPVF throughout their YSZ top coat compared to EB-PVD samples. This difference in mPVF can most likely be attributed to the difference in substrate temperatures during deposition but also could be a result of the slow heat treatments PS-PVD samples experienced.

5.1.3 Perspective

PSPVD coatings have shown promise in the efforts at developing strain tolerant coatings alternative to current EB-PVD techniques through columnar microstructure tailoring. The in situ synchrotron results demonstrate successful replication of significant characteristics of EB-PVD coatings in terms of the magnitude of YSZ/TGO interface stresses. However, the TGO morphology as well as the through-depth YSZ stress were distinctly different in the two coating types. In addition, greater variation in characteristics among the PS-PVD samples points to a need for achieving more consistency in deposition.

Additional studies investigating PS-PVD material and mechanical responses during in-situ conditions is crucial to the viability and implemenation of the TBC coating technique on turbine blades used in industry.

5.2 AM Findings

In this work, similarities and differences between residual strains of an AM lattice structure and AM solid material are found and compared to better understand the impact complex geometries such as lattice structures have on internal residual strains.

5.2.1 Lattice Structure Findings

Inconel 718 transpiration cooling lattice structures manufactured using SLM were found to have increased intensity readings compared to solid material due to the less material within the cavity containing the lattice structure. Additionally, greater variation and magnitude of strains were found within the lattice structure compared to the solid material. This is most likely due to the

greater amount of deformities found in complex geometries such as lattice structures. These deformities can potentially lead to a higher propensity of micro crack initiation in AM lattice structures compared to AM solid material.

5.2.2 Perspective

Additive manufacturing has shown extreme promise due to its ability to manufacture complex geometries. Transpiration cooling is one application that requires these complex geometries to be manufactured. These lattice structures, coupled with an increase in number of cooling holes, can provide a more uniform flow than what is found through conventional film cooling methods on turbine blades. The lattice structure has been found to obtain higher variations in residual strains compared to a solid wall of AM γ–Amdry 1718, increasing its propensity for micro-crack initiation and propagation.

Additional studies investigating the impact of cooling effectiveness on strains both parallel and perpendicular to the build direction of the AM material is needed to better understand the viability of these lattice structures to be used within the power generation and aerospace turbine industry.

LIST OF REFERENCES

[1] Rossmann, L., *Analysis of residual stress and damage mechanisms of thermal barrier coatings deposited via PS-PVD and EB-PVD*, Master's thesis, University of Central Florida, 2019.

[2] Harder, B. J. and Zhu, D., "Plasma spray-physical vapor deposition (PS-PVD) of ceramics for protective coatings," 2011.

[3] Harder, B. J., Zhu, D., Schmitt, M. P., and Wolfe, D. E., "Microstructural Effects and Properties of Non-line-of-Sight Coating Processing via Plasma Spray-Physical Vapor Deposition," *Journal of Thermal Spray Technology*, Vol. 26, No. 6, 2017, pp. 1052–1061.

[4] Schmitt, M. P., Harder, B. J., and Wolfe, D. E., "Process-structure-property relations for the erosion durability of plasma spray-physical vapor deposition (PS-PVD) thermal barrier coatings," *Surface and Coatings Technology*, Vol. 297, 2016, pp. 11–18.

[5] Shang, S.-L., Zhang, H., Wang, Y., and Liu, Z.-K., "Temperature-dependent elastic stiffness constants of α-and θ-Al2O3 from first-principles calculations," *Journal of Physics: Condensed Matter*, Vol. 22, No. 37, 2010, pp. 375403.

[6] Lunt, A., Xie, M., Baimpas, N., Zhang, S., Kabra, S., Kelleher, J., Neo, T., and Korsunsky, A., "Calculations of single crystal elastic constants for yttria partially stabilised zirconia from powder diffraction data," *Journal of Applied Physics*, Vol. 116, No. 5, 2014, pp. 053509.

[7] Butler, T., Sharma, O., Joslyn, H., and Dring, R., "Redistribution of an inlet temperature distortion in an axial flow turbine stage," *Journal of Propulsion and Power*, Vol. 5, No. 1, 1989, pp. 64–71.

[8] Holland, M. and Thake, T., "Rotor blade cooling in high pressure turbines," *Journal of aircraft*, Vol. 17, No. 6, 1980, pp. 412–418.

[9] Heidmann, J. D., Rigby, D. L., and Ameri, A. A., "A three-dimensional coupled internal/external simulation of a film-cooled turbine vane," *Journal of Turbomachinery*, Vol. 122, No. 2, 2000, pp. 348–359.

[10] Miller, R. A., "Thermal barrier coatings for aircraft engines: history and directions," *Journal of Thermal Spray Technology*, Vol. 6, No. 1, Mar 1997, pp. 35.

[11] Smith, M. F., Hall, A. C., Fleetwood, J. D., and Meyer, P., "Very low pressure plasma spray—a review of an emerging technology in the thermal spray community," *Coatings*, Vol. 1, No. 2, 2011, pp. 117–132.

[12] He, W., Mauer, G., Schwedt, A., Guillon, O., and Vaßen, R., "Advanced crystallographic study of the columnar growth of YZS coatings produced by PS-PVD," *Journal of the European Ceramic Society*, Vol. 38, No. 5, 2018, pp. 2449–2453.

[13] Yang, J., Zhao, H., Zhong, X., Ni, J., Zhuang, Y., Wang, L., and Tao, S., "Evolution of Residual Stresses in PS-PVD Thermal Barrier Coatings on Thermal Cycling," *Journal of Thermal Spray Technology*, Vol. 27, No. 6, 2018, pp. 914–923.

[14] Shao, F., Zhao, H., Zhong, X., Zhuang, Y., Cheng, Z., Wang, L., and Tao, S., "Characteristics of thick columnar YSZ coatings fabricated by plasma spray-physical vapor deposition," *Journal of the European Ceramic Society*, Vol. 38, No. 4, 2018, pp. 1930–1937.

[15] Hospach, A., Mauer, G., Vaßen, R., and Stöver, D., "Columnar-structured thermal barrier coatings (TBCs) by thin film low-pressure plasma spraying (LPPS-TF)," *Journal of thermal spray technology*, Vol. 20, No. 1-2, 2011, pp. 116–120.

[16] Gell, M., Xie, L., Ma, X., Jordan, E. H., and Padture, N. P., "Highly durable thermal barrier coatings made by the solution precursor plasma spray process," *Surface and Coatings Technology*, Vol. 177, 2004, pp. 97–102.

[17] Jordan, E. H., Xie, L., Gell, M., Padture, N., Cetegen, B., Ozturk, A., Ma, X., Roth, J., Xiao, T., and Bryant, P., "Superior thermal barrier coatings using solution precursor plasma spray," *Journal of Thermal Spray Technology*, Vol. 13, No. 1, 2004, pp. 57–65.

[18] Cernuschi, F., Lorenzoni, L., Capelli, S., Guardamagna, C., Karger, M., Vaßen, R., Von Niessen, K., Markocsan, N., Menuey, J., and Giolli, C., "Solid particle erosion of thermal spray and physical vapour deposition thermal barrier coatings," *Wear*, Vol. 271, No. 11-12, 2011, pp. 2909–2918.

[19] Padture, N. P., Gell, M., and Jordan, E. H., "Thermal barrier coatings for gas-turbine engine applications," *Science*, Vol. 296, No. 5566, 2002, pp. 280–284.

[20] Hasselman, D., Johnson, L. F., Bentsen, L. D., SYED, R., Lee, H., and SWAIN, M. V., "Thermal diffusivity and conductivity of dense polycrystalline Zr0," *Am. Ceram. Soc. Bull*, Vol. 66, No. 5, 1987, pp. 799–806.

[21] Schulz, U., Fritscher, K., Leyens, C., and Peters, M., "High-Temperature Aging of EB-PVD Thermal Barrier Coating," *CESP*, Vol. 12, No. 4, 2001, pp. 347–356.

[22] Schulz, U., "Phase transformation in EB-PVD yttria partially stabilized zirconia thermal barrier coatings during annealing," *Journal of the American Ceramic Society*, Vol. 83, No. 4, 2000, pp. 904–910.

[23] Moon, J., Choi, H., Kim, H., and Lee, C., "The effects of heat treatment on the phase transformation behavior of plasma-sprayed stabilized ZrO2 coatings," *Surface and Coatings Technology*, Vol. 155, No. 1, 2002, pp. 1–10.

[24] Brandon, J. and Taylor, R., "Phase stability of zirconia-based thermal barrier coatings part I. Zirconia-yttria alloys," *Surface and Coatings Technology*, Vol. 46, No. 1, 1991, pp. 75–90.

[25] Witz, G., Shklover, V., Steurer, W., Bachegowda, S., and Bossmann, H.-P., "Phase evolution in yttria-stabilized zirconia thermal barrier coatings studied by rietveld refinement of X-ray powder diffraction patterns," *Journal of the American Ceramic Society*, Vol. 90, No. 9, 2007, pp. 2935–2940.

[26] Rigney, D. V., Viguie, R., Wortman, D. J., and Skelly, D., "PVD thermal barrier coating applications and process development for aircraft engines," *Journal of thermal spray technology*, Vol. 6, No. 2, 1997, pp. 167–175.

[27] Veal, B. W., Paulikas, A. P., and Hou, P. Y., "Tensile stress and creep in thermally grown oxide," *Nature materials*, Vol. 5, No. 5, 2006, pp. 349.

[28] Heeg, B., Tolpygo, V. K., and Clarke, D. R., "Damage evolution in thermal barrier coatings with thermal cycling," *Journal of the American Ceramic Society*, Vol. 94, 2011, pp. s112–s119.

[29] Evans, A. G., Mumm, D., Hutchinson, J., Meier, G., and Pettit, F., "Mechanisms controlling the durability of thermal barrier coatings," *Progress in materials science*, Vol. 46, No. 5, 2001, pp. 505–553.

[30] Lee, W. Y., Stinton, D. P., Berndt, C. C., Erdogan, F., Lee, Y.-D., and Mutasim, Z., "Concept of functionally graded materials for advanced thermal barrier coating applications," *Journal of the American Ceramic Society*, Vol. 79, No. 12, 1996, pp. 3003–3012.

[31] Rabiei, A. and Evans, A., "Failure mechanisms associated with the thermally grown oxide in plasma-sprayed thermal barrier coatings," *Acta materialia*, Vol. 48, No. 15, 2000, pp. 3963–3976.

[32] Liu, J., "Mechanisms Of Lifetime Improvement In Thermal Barrier Coatings With Hf And/or Y Modification Of Cmsx-4 Superalloy Substrates," 2007.

[33] Yang, L., Yang, F., Long, Y., Zhao, Y., Xiong, X., Zhao, X., and Xiao, P., "Evolution of residual stress in air plasma sprayed yttria stabilised zirconia thermal barrier coatings after isothermal treatment," *Surface and Coatings Technology*, Vol. 251, 2014, pp. 98–105.

[34] Alam, M. Z., Satyanarayana, D., Chatterjee, D., Sarkar, R., and Das, D., "Creep behavior of Pt-aluminide (PtAl) coated directionally solidified Ni-based superalloy CM-247LC after thermal exposure," *Materials Science and Engineering: A*, Vol. 641, 2015, pp. 84–95.

[35] Steenbakker, R., "Phosphor thermometry in an EB-PVD TBC," 2008.

[36] Hayashi, S., Ford, S., Young, D., Sordelet, D., Besser, M., and Gleeson, B., "α-NiPt (Al) and phase equilibria in the Ni–Al–Pt system at 1150 C," *Acta Materialia*, Vol. 53, No. 11, 2005, pp. 3319–3328.

[37] Weyant, C., Almer, J., and Faber, K., "Through-thickness determination of phase composition and residual stresses in thermal barrier coatings using high-energy X-rays," *Acta materialia*, Vol. 58, No. 3, 2010, pp. 943–951.

[38] Gong, X.-Y. and Clarke, D., "On the measurement of strain in coatings formed on a wrinkled elastic substrate," *Oxidation of metals*, Vol. 50, No. 5-6, 1998, pp. 355–376.

[39] Sridharan, S., Xie, L., Jordan, E. H., and Gell, M., "Stress variation with thermal cycling in the thermally grown oxide of an EB-PVD thermal barrier coating," *Surface and Coatings Technology*, Vol. 179, No. 2-3, 2004, pp. 286–296.

[40] Schlichting, K. W., Padture, N., Jordan, E., and Gell, M., "Failure modes in plasma-sprayed thermal barrier coatings," *Materials Science and Engineering: A*, Vol. 342, No. 1-2, 2003, pp. 120–130.

[41] Li, C., Zhang, X., Chen, Y., Carr, J., Jacques, S., Behnsen, J., Di Michiel, M., Xiao, P., and Cernik, R., "Understanding the residual stress distribution through the thickness of atmosphere plasma sprayed (APS) thermal barrier coatings (TBCs) by high energy synchrotron XRD; digital image correlation (DIC) and image based modelling," *Acta Materialia*, Vol. 132, 2017, pp. 1–12.

[42] Von Niessen, K. and Gindrat, M., "Plasma spray-PVD: a new thermal spray process to deposit out of the vapor phase," *Journal of thermal spray technology*, Vol. 20, No. 4, 2011, pp. 736–743.

[43] Dinwiddie, R. B., Beecher, S. C., Porter, W. D., and Nagaraj, B. A., "The effect of thermal aging on the thermal conductivity of plasma sprayed and EB-PVD thermal barrier coatings," Tech. rep., Oak Ridge National Lab., TN (United States), 1996.

[44] Teixeira, V., Andritschky, M., Fischer, W., Buchkremer, H., and Stöver, D., "Effects of deposition temperature and thermal cycling on residual stress state in zirconia-based thermal barrier coatings," *Surface and Coatings Technology*, Vol. 120, 1999, pp. 103–111.

[45] Zhao, H., Yu, F., Bennett, T. D., and Wadley, H. N., "Morphology and thermal conductivity of yttria-stabilized zirconia coatings," *Acta Materialia*, Vol. 54, No. 19, 2006, pp. 5195–5207.

[46] Bernard, B., Quet, A., Bianchi, L., Joulia, A., Malié, A., Schick, V., and Rémy, B., "Thermal insulation properties of YSZ coatings: suspension plasma spraying (SPS) versus electron beam physical vapor deposition (EB-PVD) and atmospheric plasma spraying (APS)," *Surface and Coatings Technology*, Vol. 318, 2017, pp. 122–128.

[47] Bunker, R. S., "Cooling design analysis," *The Gas Turbine Handbook, US Department of Energy NETL, Morgantown, VA*, 2006.

[48] Tomimatsu, T., Kagawa, Y., and Zhu, S., "Residual stress distribution in electron beam-physical vapor deposited ZrO 2 thermal barrier coating layer by raman spectroscopy," *Metallurgical and Materials Transactions A*, Vol. 34, No. 8, 2003, pp. 1739–1741.

[49] Mauer, G., Hospach, A., and Vaßen, R., "Process development and coating characteristics of plasma spray-PVD," *Surface and Coatings Technology*, Vol. 220, 2013, pp. 219–224.

[50] Von Niessen, K., Gindrat, M., and Refke, A., "Vapor phase deposition using plasma spray-PVD™," *Journal of thermal spray technology*, Vol. 19, No. 1-2, 2010, pp. 502–509.

[51] Refke, A., Damani, R., et al., "LPPS Thin film: a hybrid coating technology between thermal spray and pvd for functional thin coatings and large area applications," *2007*, 2007, pp. A–X.

[52] Dorier, J.-L., Gindrat, M., Hollenstein, C., Loch, M., Refke, A., Salito, A., and Barbezat, G., "Plasma jet properties in a new spraying process at low pressure for large area thin film deposition," Tech. rep., 2001.

[53] Spinhirne, N. R., *The Development and Characterization of Novel Yttria-Stabilized Zirconia Coatings Deposited by Very Low Pressure Plasma Spray*, Ph.D. thesis, New Mexico Institute of Mining and Technology, 2008.

[54] Yang, J., Zhao, H., Zhong, X., Shao, F., Liu, C., Zhuang, Y., Ni, J., and Tao, S., "Thermal cycling behavior of quasi-columnar YSZ coatings deposited by PS-PVD," *Journal of Thermal Spray Technology*, Vol. 26, No. 1-2, 2017, pp. 132–139.

[55] Gell, M., Vaidyanathan, K., Barber, B., Jordan, E., and Cheng, J., "Mechanism of spallation in platinum aluminide/electron beam physical vapor-deposited thermal barrier coatings," *Metallurgical and Materials Transactions A*, Vol. 30, No. 2, 1999, pp. 427–435.

[56] Hernandez, M. T., Karlsson, A. M., and Bartsch, M., "On TGO creep and the initiation of a class of fatigue cracks in thermal barrier coatings," *Surface and Coatings Technology*, Vol. 203, No. 23, 2009, pp. 3549–3558.

[57] Almer, J., Lienert, U., Peng, R. L., Schlauer, C., and Odén, M., "Strain and texture analysis of coatings using high-energy X-rays," *Journal of applied physics*, Vol. 94, No. 1, 2003, pp. 697–702.

[58] Thornton, J., Slater, S., and Almer, J., "The Measurement of Residual Strains Within Thermal Barrier Coatings Using High-Energy X-Ray Diffraction," *Journal of the American Ceramic Society*, Vol. 88, No. 10, 2005, pp. 2817–2825.

[59] Hauk, V., *Structural and residual stress analysis by nondestructive methods: Evaluation-Application-Assessment*, Elsevier, 1997.

[60] Bunker, R. S., "A review of shaped hole turbine film-cooling technology," *Journal of heat transfer*, Vol. 127, No. 4, 2005, pp. 441–453.

[61] Esgar, J. B., "Turbine cooling-its limitations and its future," 1970.

[62] Halls, G., "Air Cooling of Turbine Blades and Vanes: An account of the history and development of gas turbine cooling," *Aircraft Engineering and Aerospace Technology*, Vol. 39, No. 8, 1967, pp. 4–14.

[63] Ealy, B., Calderon, L., Wang, W., Valentin, R., Mingareev, I., Richardson, M., and Kapat, J., "Characterization of laser additive manufacturing-fabricated porous superalloys for turbine components," *Journal of Engineering for Gas Turbines and Power*, Vol. 139, No. 10, 2017, pp. 102102.

[64] Thorstenson, R. A., "Combustor liner cooling arrangement," Nov. 30 1971, US Patent 3,623,711.

[65] Herdy Jr, J. R., Kamel, M. R., and Lopata, J. B., "Transpiration cooling of rocket engines," Aug. 19 2003, US Patent 6,606,851.

[66] Uriondo, A., Esperon-Miguez, M., and Perinpanayagam, S., "The present and future of additive manufacturing in the aerospace sector: A review of important aspects," *Proceedings of the Institution of Mechanical Engineers, Part G: Journal of Aerospace Engineering*, Vol. 229, No. 11, 2015, pp. 2132–2147.

[67] Mingareev, I., Bonhoff, T., El-Sherif, A. F., and Richardson, M., "Femtosecond laser post-processing of metal parts produced by laser additive manufacturing," *MATEC Web of Conferences*, Vol. 8, EDP Sciences, 2013, p. 02010.

[68] Moiz, M., *The influence of grain size on the mechanical properties of Inconel 718*, Master's thesis, Linköping University, 2013.

[69] Henninger, S., *Phase analyses of additively manufactured Ni-base alloy IN718 by means of in-situ synchrotron X-ray diffraction*, Master's thesis, Freidrich-Alexander Universität Erlangen-Nürnberg, 2019.

[70] Gaynor, A. T., Meisel, N. A., Williams, C. B., and Guest, J. K., "Topology optimization for additive manufacturing: considering maximum overhang constraint," *15th AIAA/ISSMO multidisciplinary analysis and optimization conference*, 2014, p. 2036.

[71] Makki, Y. and Jakubowski, G., "An experimental study of film cooling from diffused trapezoidal shaped holes," *4th Thermophysics and Heat Transfer Conference*, 1986, p. 1326.

[72] Gritsch, M., Schulz, A., and Wittig, S., "Adiabatic wall effectiveness measurements of film-cooling holes with expanded exits," *Journal of Turbomachinery*, Vol. 120, No. 3, 1998, pp. 549–556.

[73] Saumweber, C., Schulz, A., and Wittig, S., "Free-stream turbulence effects on film cooling with shaped holes," *Journal of turbomachinery*, Vol. 125, No. 1, 2003, pp. 65–73.

[74] Schmidt, D. L., Sen, B., and Bogard, D. G., "Film cooling with compound angle holes: adiabatic effectiveness," *Journal of turbomachinery*, Vol. 118, No. 4, 1996, pp. 807–813.

[75] Adam, J. and Cox, B., "The irradiation-induced phase transformation in zirconia solid solutions," *Reactor Sci.*, Vol. 11, 1959.

[76] He, B. B., "Introduction to two-dimensional X-ray diffraction," *Powder diffraction*, Vol. 18, No. 2, 2003, pp. 71–85.

[77] Kotowicz, J., Job, M., Brzeczek, M., Nawrat, K., and Medrych, J., "The methodology of the gas turbine efficiency calculation," *Archives of Thermodynamics*, Vol. 37, No. 4, 2016, pp. 19–35.

[78] Xu, L., Bo, S., Hongde, Y., and Lei, W., "Evolution of Rolls-Royce air-cooled turbine blades and feature analysis," *Procedia Engineering*, Vol. 99, 2015, pp. 1482–1491.

[79] Knipe, K., Manero II, A., Siddiqui, S. F., Meid, C., Wischek, J., Okasinski, J., Almer, J., Karlsson, A. M., Bartsch, M., and Raghavan, S., "Strain response of thermal barrier coatings captured under extreme engine environments through synchrotron X-ray diffraction," *Nature communications*, Vol. 5, 2014, pp. 4559.

[80] Knipe, K., Manero, A. C., Sofronsky, S., Okasinski, J., Almer, J., Wischek, J., Meid, C., Karlsson, A., Bartsch, M., and Raghavan, S., "Synchrotron X-Ray Diffraction Measurements Mapping Internal Strains of Thermal Barrier Coatings During Thermal Gradient Mechanical Fatigue Loading," *Journal of Engineering for Gas Turbines and Power*, Vol. 137, No. 8, 2015, pp. 082506.

[81] Manero, A., Knipe, K., Wischek, J., Meid, C., Okasinski, J., Almer, J., Karlsson, A., Bartsch, M., and Raghavan, S., "Capturing the Competing Influence of Thermal and Mechanical Loads on the Strain of Turbine Blade Coatings via High Energy X-rays," *Coatings*, Vol. 8, No. 9, 2018, pp. 320.

[82] Siddiqui, S. F., Knipe, K., Manero, A., Meid, C., Wischek, J., Okasinski, J., Almer, J., Karlsson, A. M., Bartsch, M., and Raghavan, S., "Synchrotron X-ray measurement techniques for thermal barrier coated cylindrical samples under thermal gradients," *Review of Scientific Instruments*, Vol. 84, No. 8, 2013, pp. 083904.

[83] Manero, A., Sofronsky, S., Knipe, K., Meid, C., Wischek, J., Okasinski, J., Almer, J., Karlsson, A. M., Raghavan, S., and Bartsch, M., "Monitoring local strain in a thermal barrier coating system under thermal mechanical gas turbine operating conditions," *JOM*, Vol. 67, No. 7, 2015, pp. 1528–1539.

[84] Almer, J. and Stock, S., "Internal strains and stresses measured in cortical bone via high-energy X-ray diffraction," *Journal of structural biology*, Vol. 152, No. 1, 2005, pp. 14–27.

[85] Manns, T. and Scholtes, B., "DECcalc - A Program for the Calculation of Diffraction Elastic Constants from Single Crystal Coefficients," *Residual Stresses VIII*, Vol. 681 of *Materials Science Forum*, Trans Tech Publications, 5 2011, pp. 417–419.

[86] Noyan, I. C. and Cohen, J. B., *Residual stress: measurement by diffraction and interpretation*, Springer, 2013.

[87] Garvie, R. C. and Nicholson, P. S., "Phase analysis in zirconia systems," *Journal of the American Ceramic Society*, Vol. 55, No. 6, 1972, pp. 303–305.

[88] Toraya, H., Yoshimura, M., and Somiya, S., "Calibration curve for quantitative analysis of the Monoclinic-Tetragonal ZrO2 system by X-ray diffraction," *Journal of the American Ceramic Society*, Vol. 67, No. 6, 1984, pp. C–119.

[89] Cihak, U., Staron, P., Clemens, H., Homeyer, J., Stockinger, M., and Tockner, J., "Characterization of residual stresses in turbine discs by neutron and high-energy X-ray diffraction and comparison to finite element modeling," *Materials Science and Engineering: A*, Vol. 437, No. 1, 2006, pp. 75–82.

[90] Evans, A., He, M., and Hutchinson, J., "Mechanics-based scaling laws for the durability of thermal barrier coatings," *Progress in materials science*, Vol. 46, No. 3-4, 2001, pp. 249–271.

[91] Tolpygo, V., Clarke, D., and Murphy, K., "Oxidation-induced failure of EB-PVD thermal barrier coatings," *Surface and coatings technology*, Vol. 146, 2001, pp. 124–131.

[92] Zhu, W., Cai, M., Yang, L., Guo, J., Zhou, Y., and Lu, C., "The effect of morphology of thermally grown oxide on the stress field in a turbine blade with thermal barrier coatings," *Surface and Coatings Technology*, Vol. 276, 2015, pp. 160–167.

[93] Peters, M., Leyens, C., Schulz, U., and Kaysser, W. A., "EB-PVD thermal barrier coatings for aeroengines and gas turbines," *Advanced engineering materials*, Vol. 3, No. 4, 2001, pp. 193–204.

[94] Vaßen, R., Traeger, F., and Stöver, D., "Correlation between spraying conditions and microcrack density and their influence on thermal cycling life of thermal barrier coatings," *Journal of thermal spray technology*, Vol. 13, No. 3, 2004, pp. 396–404.

[95] Braue, W., "Environmental stability of the YSZ layer and the YSZ/TGO interface of an in-service EB-PVD coated high-pressure turbine blade," *Journal of materials science*, Vol. 44, No. 7, 2009, pp. 1664.

[96] Zhao, X., Wang, X., and Xiao, P., "Sintering and failure behaviour of EB-PVD thermal barrier coating after isothermal treatment," *Surface and Coatings Technology*, Vol. 200, No. 20-21, 2006, pp. 5946–5955.

[97] Tanaka, M., Kitazawa, R., Tomimatsu, T., Liu, Y., and Kagawa, Y., "Residual stress measurement of an EB-PVD Y2O3-ZrO2 thermal barrier coating by micro-Raman spectroscopy," *Surface and Coatings Technology*, Vol. 204, No. 5, 2009, pp. 657–660.

[98] Viazzi, C., Bonino, J.-P., Ansart, F., and Barnabé, A., "Structural study of metastable tetragonal YSZ powders produced via a sol–gel route," *Journal of Alloys and Compounds*, Vol. 452, No. 2, 2008, pp. 377–383.

[99] Mevrel, R., Rio, C., Poulain, M., Diot, C., and Nardou, F., "Technical Report No. 28/2019M," 1987.

[100] Galetz, M. C., "Coatings for superalloys," *Superalloys*, InTech, 2015, pp. 277–298.

[101] Tolpygo, V. and Clarke, D., "Tensile cracking during thermal cycling of alumina films formed by high-temperature oxidation," *Acta materialia*, Vol. 47, No. 13, 1999, pp. 3589–3605.

[102] Fritscher, K., Szücs, F., Schulz, U., Saruhan, B., and Kaysser, W., "Impact on Thermal Exposure of EB-PVD-TBCs on Young's Modulus and Sintering," *CESP*, Vol. 23, No. 4, 2002, pp. 341–352.